


Article

Numerical Simulation of Pre-Reduction for a New Process of Acid Production from Phosphogypsum by Gas Sulfur Reduction

Yanxin Chen , Xuyang Fan, Bo Zhao and Leilei Zhang

College of Materials Science and Engineering, Xi'an University of Architecture and Technology, Xi'an 710055, China

* Correspondence: chenyanxin@xauat.edu.cn; Tel.: +86-29-8550-2390

Abstract: The gas sulfur reduction of phosphogypsum in the acid co-production of sulfoaluminate cement clinker is a new process for treating phosphogypsum. The reduction furnace of this system was studied and analyzed by combining computational fluid dynamics (CFD) and experimental validation. The effects of $n(\text{CaSO}_4)/n(\text{S}_2)$, particle residence time, and kiln tail flue gas temperature on the performance of the reduction furnace were obtained. A second-order response model based on the response surface methodology was developed using a three-factor Box–Behnken design (BBD). The results show that the comparison error between the simulation and test data of the reduction furnace is acceptable. The above three conditions arranged in order of significance in terms of their effect on the performance of the reduction furnace is $n(\text{CaSO}_4)/n(\text{S}_2) > \text{particle residence time} > \text{kiln tail gas temperature}$. Finally, by optimizing the response surface model, the predicted optimal operation parameter combination is $n(\text{CaSO}_4)/n(\text{S}_2) = 3.04$, with the particle residence time and flue gas temperature at the kiln end given as 8.90 s and 1265.39 K, respectively.

Keywords: gas sulfur reduction of phosphogypsum; reduction furnace; numerical simulation; experimental verification; gas–solid reaction; response surface model



Citation: Chen, Y.; Fan, X.; Zhao, B.; Zhang, L. Numerical Simulation of Pre-Reduction for a New Process of Acid Production from Phosphogypsum by Gas Sulfur Reduction. *Processes* **2023**, *11*, 972. <https://doi.org/10.3390/pr11030972>

Academic Editors: Ahmed Elwardany, Mahmoud Omar Amer and Kai Yan

Received: 21 February 2023

Revised: 20 March 2023

Accepted: 21 March 2023

Published: 22 March 2023



Copyright: © 2023 by the authors. Licensee MDPI, Basel, Switzerland. This article is an open access article distributed under the terms and conditions of the Creative Commons Attribution (CC BY) license (<https://creativecommons.org/licenses/by/4.0/>).

1. Introduction

Phosphogypsum is the main by-product produced in the process of phosphoric acid production. Its main component is calcium sulfate dihydrate ($\text{CaSO}_4 \cdot 2\text{H}_2\text{O}$), the content thereof which reaches more than 90%. Phosphogypsum is an important gypsum resource [1,2]. Compared to natural gypsum, phosphogypsum is limited in its comprehensive use in the construction materials industry and enterprises involved in the development of phosphorus chemicals because it contains small amounts of free phosphoric acid and its salts, organic matter, and other impurities [3].

Several studies have shown that phosphogypsum pyrolysis products sulfur dioxide (SO_2) and calcium oxide (CaO) can make acid and replace some calcium raw materials in cement production [4,5]. However, the reaction temperature for the direct decomposition of phosphogypsum is as high as 1573 K [6,7], with a decomposition rate of only 36.2%. To increase the decomposition rate of phosphogypsum while reducing the reaction temperature, researchers have used reducing media. Furthermore, they used coke and activated carbon as reducing agents to decompose phosphogypsum. Its decomposition rate was more than 80%, while the reaction temperature reduced by 323 K [8,9]. However, the reaction process was accompanied by complex side reactions and large amounts of carbon emission. These are extremely detrimental to the ecological environment and subsequent SO_2 collection process for acid production. Benhe et al. [10] used sulfur as a reducing agent to decompose phosphogypsum and discovered that it had advantages, such as low reaction temperature and large SO_2 concentration within the homogeneous reduction system.

Jiandong et al. [11] explained the microscopic reaction mechanism of the interaction between the sulfur and phosphogypsum surface through their research on the technology of producing sulfuric acid by the sulfur chemical cycle combustion of phosphogypsum. In particular, they indicated that CaSO_4 has a high chemical reactivity as an oxygen carrier. Through thermodynamic simulation and experimental research, Xiushan et al. [12] showed that the first-step reaction temperature of the sulfur reduction of phosphogypsum was 993 K, and the reaction product met the subsequent material ratio. Xinlong et al. [13] built a process pilot plant using sulfur decomposition phosphogypsum acid production technology and the product performance was reliable. However, it still had defects, such as a reaction residence time of up to 60 min and low sulfur indirect heat exchange efficiency.

After years of theoretical research and experimental demonstration, the Powder Engineering Research Institute of Xi'an University of Architecture and Technology has developed a new process for CaSO_4 decomposition using sulfur reduction outside the kiln. In the process, the partial reduction of the calcium sulfate is accomplished in the suspension reduction furnace outside the kiln, where gaseous sulfur is used to reduce the calcium sulfate to produce calcium sulfide and sulfur dioxide. Further reaction of the calcium sulfate with calcium sulfide to produce calcium oxide and sulfur dioxide is conducted in the kiln. This significantly increased the reaction efficiency of the system and reduced the material residence time in the calcining kiln by 30 min. Homogeneous chemical element reduction can increase the purity of SO_2 in the system, while effectively reducing the carbon emissions and production costs of the kiln and improving production efficiency. The reduction furnace is the core equipment of pre-reduction outside the kiln. Numerical simulation of the gas–solid phase reaction process in the reduction furnace has been used to obtain parameters related to furnace-side flow, heat exchange, and decomposition, which provides a reference for the study of numerical simulation methods in the field of phosphogypsum gas sulfur reduction [14,15].

Numerical simulations have been widely used in the design and optimization of pre-reduction furnaces owing to the increasing development of computational fluid dynamics (CFD) methods. Lyu et al. [16] used particle-centered averaging to average the variables of discrete phases, thereby avoiding the errors of the standard Euler–Euler model based on the phase averaging method. This method was proven to reduce the peak gas volume fraction under the wall peak and fine dispersion flow by comparing both methods. The over-prediction of the peak gas volume fraction at the wall and fine dispersion flows was demonstrated by comparing both methods. Mao et al. [17] used the Euler–Euler method to simulate the decomposition of CaCO_3 during calcination in cement production, wherein heavy oil was defined as a discrete phase and the other components as continuous phases. The heat, mass, momentum, species, and energy transport between these different phases were calculated based on the phase interaction coefficients and model. This revealed that the numerical predictions corresponded with the production line data. Yang et al. [18] used the discrete phase model (DPM) based on the Euler–Lagrange method to accurately describe the NO generation process in the reduction furnace, wherein the accuracy of the computational model was demonstrated. Nakhaei et al. [19] studied the gas–solid flow of cold particles and heated air in the calciner of a pilot system using the Euler–Lagrange and multiphase particle-in-cell method (MP-PIC). The accuracy of two resistance models, EMMS and Gidaspow, was compared using the gas temperature distribution in different regions. Gao et al. [20] established a Euler–Lagrange model for a reduction furnace using the MP-PIC method and studied the coupling reaction of raw material and fuel in the reduction furnace by zoning. They found that there are three spray effects and five recirculation zones near the feedstock inlet, and also obtained optimal conditions for biomass incorporation in the reduction furnace. Regarding multiphase flow models, the Eulerian multiphase flow model best describes multiple independent yet interacting phases [21]. Zhang et al. [22] used a modified Eulerian two-fluid model to simulate a gas–liquid multiphase flow dynamic pump. The effect of multiphase mixing on the operation in the pump is described by the gas void rate and phase interaction gas content rate

characteristics, respectively. Unlike the Eulerian multiphase flow, the component transport model better simulates the interaction between the components of the mixture and other phases [23]. Pandey et al. [24] used a DPM based on the Eulerian–Lagrange method, which was applied to a gasifier. It investigated several gasification parameters by implementing an alternative chemical kinetic scheme, which was validated by different equivalence ratios. Nathada et al. [21] analyzed a downdraft gasifier using a two-dimensional CFD model. They predicted the effect of the key design parameters, such as the throat diameter and height of the air nozzle on the performance of the equipment, and obtained its optimal parameters. Mei et al. [25] conducted a numerical simulation of the coupling of fuel combustion and calcium carbonate decomposition in a vortex pre-reduction furnace and analyzed the combustion characteristics of pulverized coal, while exploring its coupling with raw meal. The accuracy of the component transport model was demonstrated by comparing the predicted data with actual working conditions. The above studies show that the component transport model was more suitable for simulating the multiphase mixing state in a reduction furnace.

In this study, the main equipment and actual test conditions of the new phosphogypsum reduction process outside the sulfur gas kiln were determined and a 1:1 suspension reduction furnace model was established using Fluent software. On the one hand, the multiphase flow uses the component transport model in the Euler–Lagrange system. On the other hand, the chemical reaction uses the finite rate/vortex dissipation model to simulate the multiphase reaction process of CaSO_4 decomposition in the suspension reduction furnace of the system. This provides basic knowledge of the process and equipment structure of the suspension reduction furnace. This also provides a reference for the study of numerical simulation methods in the field of the gas sulfur reduction of phosphogypsum.

2. Physical Model

The internal structure of the reduction furnace of the sulfur gas reduction phosphogypsum system, geometric model, and mesh division are shown in Figure 1. The reduction furnace is an external circulation-type with a high solid-to-gas ratio. The kiln tail flue gas enters from the reduction furnace bottom indentation. The raw material and sulfur gas inlets are located in the lower section on both sides of the reduction furnace, and the airflow enters the cyclone separator tangentially at the top of the reduction furnace. Because the computational flow field is complex with multiphase flow chemistry, the mesh quality determines the computational convergence speed and simulation accuracy directly. Hence, Fluent meshing was used to divide the above geometric model into a mixed tetrahedral–hexahedral mesh and encrypt the local mesh for each inlet to better capture the calculation results.

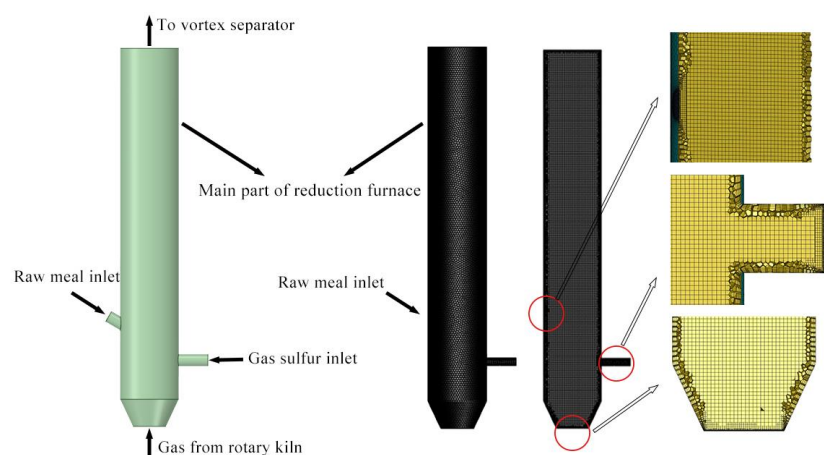


Figure 1. Structure, grid, and local densification diagram of reduction furnace.

3. Mathematical Models and Numerical Solution Methods

With the rapid development of computational simulation technology and continuous improvement of numerical methods, the numerical simulation method has gradually become an important method in investigating multiphase flow. CFD uses three fundamental physics laws: conservation of mass, energy, and momentum. For turbulent flows with chemical reactions or mixtures of different components, the system must use the conservation of components and turbulent transport equations [26]. The control (the conservation laws) is described by mathematical equations, and the corresponding control equations for each conservation law are detailed in the following subsections.

3.1. Research Hypothesis

As the specific reaction process between the sulfur and raw meal particles in the reduction furnace is complex, to study the interactions, we make the following assumptions regarding the actual operating conditions of the reduction furnace.

- (1) Select a pressure based solver, and the flow field is steady, i.e., during the stable operation of the reduction furnace, the variable parameters do not change with time in the reversing cycle.
- (2) Except for all the inlets and outlets such as the kiln tail gas inlet, gas sulfur inlet, and raw meal inlet, the other parts of the reduction furnace are modelled with non-slip wall and no energy loss conditions.
- (3) The fluid flow is viscous Newtonian fluid turbulent flow.
- (4) Some of the physical parameters of the flue gas in the reduction furnace, such as the specific heat capacity and thermal conductivity, are set using the default values.
- (5) The flow in the flow field occurs in a hot environment, heat and mass transfer between the gas and solid phases is considered, and viscous heat is ignored.
- (6) The composition of the raw meal particles is simplified as calcium sulfate, and the main chemical reaction occurring in the reduction furnace is the reaction of the gas sulfur and calcium sulfate.
- (7) Both gas and solids flow out of the calculation area from the outlet.

3.2. Mathematical Models

3.2.1. Turbulence Model

The SST k - ω turbulence model is a two-equation hybrid model. Proposed by Menter [27] in 1994, it combines the advantages of the k - ω and k - ϵ models, while compensating for the shortcomings of both models. The model uses the k - ω and k - ϵ formulations for simulations near the boundary layer and calculations in fully developed fluid regions, respectively. This is owing to the sensitivity of k - ω formulation to inlet free-flow turbulence. The generalized control equation for the SST k - ω turbulence model is expressed as:

$$\frac{\partial}{\partial t}(\rho k) + \frac{\partial}{\partial x_i}(\rho k u_i) = \frac{\partial}{\partial x_j} \left(\Gamma_k \frac{\partial k}{\partial x_j} \right) + F_k - Y_k \quad (1)$$

$$\frac{\partial}{\partial t}(\rho \omega) + \frac{\partial}{\partial x_i}(\rho \omega u_i) = \frac{\partial}{\partial x_j} \left(\Gamma_\omega \frac{\partial \omega}{\partial x_j} \right) + F_\omega - Y_\omega + D_\omega \quad (2)$$

where k is the turbulent kinetic energy, t is the time, ρ is the density, u_i and u_j are the mean values of the turbulent velocity, x_i and x_j are the coordinate components, ω is the turbulent special dissipation, Γ_k and Γ_ω are the effective diffusion coefficients, F_k and F_ω are the turbulence generation terms, Y_k and Y_ω are the dissipation terms of k and ω , and D_ω is the diffusion term.

3.2.2. Discrete Phase Model

The model was selected to track the trajectory of particles in a continuous-phase Eulerian coordinate system using the Lagrange method, also known as DPM. Because the

flow in the furnace is strongly turbulent, the effect of turbulent pulsations on the particle population orbit is calculated using a stochastic orbit model [28]. Considering the effects of gravity and traction, while neglecting the effects of other forces, the equilibrium equation for the forces acting on the particles in the Cartesian coordinate system (x-direction) is expressed as:

$$\frac{du_p}{dt} = F_D(u - u_p) + \frac{g_x(\rho_p - \rho)}{\rho_p} + F_x \quad (3)$$

$$F_D = \frac{18\mu}{\rho_p d_p^2} \frac{C_D \text{Re}}{24} \quad (4)$$

$$\text{Re} = \frac{\rho d_p |u_p - u|}{\mu} \quad (5)$$

$$C_D = a_1 + \frac{a_2}{\text{Re}} + \frac{a_3}{\text{Re}} \quad (6)$$

where $F_D(u - u_p)$ denotes the traction force per unit mass of the particle, u is the fluid phase velocity, u_p is the particle velocity, μ is the hydrodynamic viscosity, ρ is the fluid density, ρ_p is the particle density, d_p is the particle diameter, and Re is the particle Reynolds number. C_D is the traction coefficient. For spherical particles, a_1 , a_2 , and a_3 are constants within a Reynolds number range of 0.28, 6, and 21, respectively.

3.2.3. Gas–Solid Chemical Reaction Model

The chemical reactions of raw material particles occur in the furnace under sulfur gas reduction. Hence, the turbulent chemical reaction model was chosen as a generic finite rate model, i.e., the mass fraction of each substance was predicted by solving the component conservation equations of the chemical substances [29]. The generalized form of the conservation equation is expressed as follows:

$$\frac{\partial}{\partial t}(\rho Y_t) + \nabla(\rho \bar{v} Y_t) = -\nabla \bar{J}_t + R_t + S_t \quad (7)$$

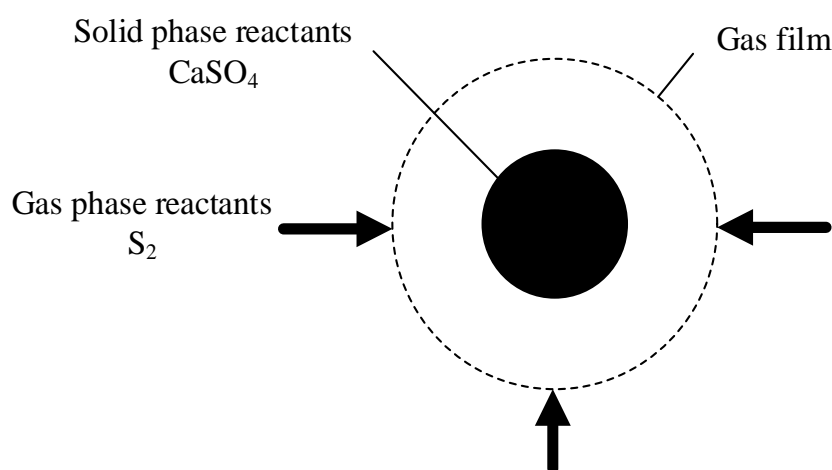
where Y_t is the mass fraction of substance i , R_t is the net rate of the chemical reaction production, and S_t is the additional rate of production in the discrete phase. If there are N substances in the system, the $N-1$ equations must be solved. The sum of the mass fractions of N substances is 1, and the mass fraction of the N th substance is obtained by subtraction. Hence, the N th substance must be the one with the largest mass fraction to minimize the numerical error. The interaction of turbulent chemical reactions is modeled using the vortex dissipation conceptual model, which allows the careful Arrhenius chemical kinetics to merge in turbulence, thereby simultaneously increasing the computational cost [30].

The homogeneous flow model in the reduction furnace is adapted to a more extreme situation. The gas–solid phase mass and heat transfer processes must be fully considered in industrial applications. Hence, the non-homogeneous flow model is more suitable. In the reduction furnace simulation study, the gas–solid phase is modelled as two independent phases. Regarding the existence of the interpenetration phenomenon, previous research has developed a nucleation model, particle model, homogeneous reaction model, structural pore model, and other reaction models applicable to non-homogeneous flow structures. The characteristics of the different gas–solid reaction models are shown in Table 1.

Table 1. Characteristics of different gas–solid reaction models.

Model	Characteristic
Sohn and Szekely [31]; shrinking-core model	The reaction gradually advances from the outer surface of the particle to the core part. However, the particle volume remains unchanged, which is suitable for describing the roasting and reduction of dense particles, such as sulfide ore.
Szekely et al. [32]; particle model	The reaction takes place in a region rather than at an interface, which is suitable for porous solid particles with a large porosity.
Borgwardt [33]; uniform reaction model	The reaction is uniformly carried out in the whole particle. The diffusion rate of the gas phase through the solid particle is faster than the reaction rate. The internal diffusion control reaction can be uniformly carried out in the reaction, which is suitable for fine particles.
Keener and Khang [34]; pore structure model	The effect of pore structure parameters on the reaction rate is described. It is suitable for describing the internal processes of particles, such as fuel desulfurization.

Sohn et al. [31] first proposed a nucleation model that was used to describe the chemistry of adsorbed gases on porous particles. As shown in Figures 2 and 3, the microscopic physicochemical steps in this gas–solid reaction model are similar to those of other models and are usually divided into five steps [35]. (1) The gas-phase molecules diffuse from the gas-phase main body to the outer surface of solid-phase particles via an external diffusion process. (2) Gas-phase molecules on the surface of solid-phase particles further diffuse through the particle pores (an internal diffusion process). (3) Gas-phase molecules undergo chemical reactions on the surface of local solid-phase particles (a surface reaction process). (4) Reactant molecules diffuse through the product layer and then further react. (5) Solid products gradually grow, leading to solid-phase particle structure changes. These steps proceed simultaneously and are mutually constrained. It is a typical multiscale, multiple physicochemical coupled system.

**Figure 2.** Reaction model of sulfur gas and CaSO_4 .

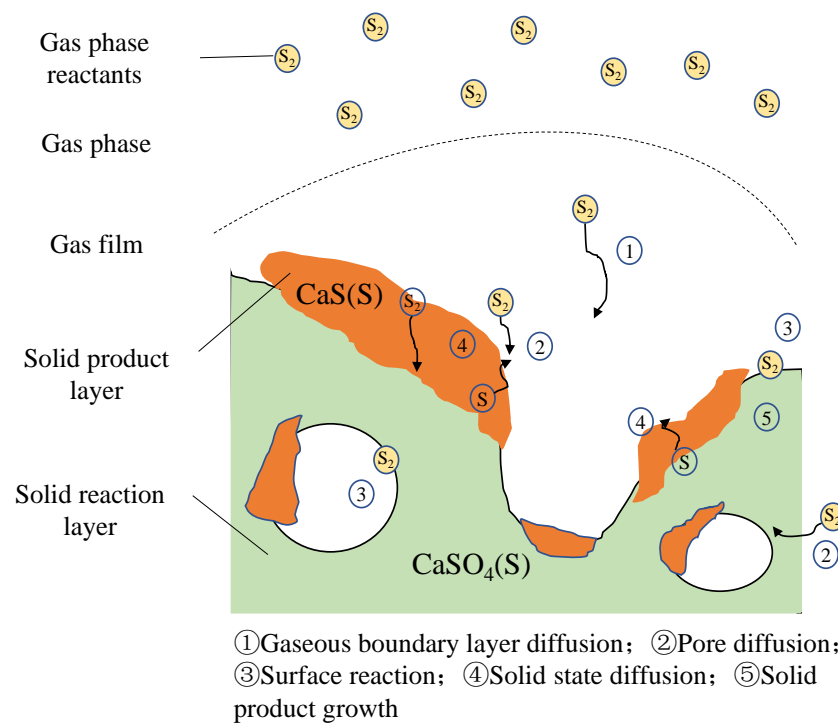


Figure 3. Physical and chemical steps of gas–solid reaction.

The reaction between gaseous sulfur and CaSO_4 in the reduction furnace is a gas–solid non-catalytic non-homogeneous reaction. Its reaction model is based on the nucleation model of the gas–solid reaction (Equation (8)), wherein the solid-phase reactant nuclei are wrapped with a gas film, while gaseous sulfur reacts with CaSO_4 through the gas film as expressed below:



In this model, the solid-phase particle diameter remains constant during the reduction of CaSO_4 particles by gaseous sulfur, while the particle density decreases. The reaction rate is expressed as:

$$t = \frac{\rho_s R_0}{c_{A,0} - c_{A,e}} \left\{ \frac{f}{3\beta} + \frac{R_0}{6D_{AB,e}} \left[1 - 3(1-f)^{2/3} + 2(1-f) \right] + \frac{K}{k(1+K)} \left[1 - (1-f)^{1/3} \right] \right\} \quad (9)$$

where ρ_s is the density of gaseous sulfur within the CaSO_4 particles (mol/m^3), R_0 is the particle size, $c_{A,0}$ and $c_{A,e}$ are the equilibrium concentrations of gaseous sulfur at the beginning and end of the reaction, respectively (mol/m^3), f is the conversion rate, β is the gas film mass transfer coefficient (m/s), $D_{AB,e}$ is the effective diffusion coefficient (m^2/s), k is the rate constant of the primary reversible reaction, and K is the reaction equilibrium constant.

The first, second, and third terms in parentheses are the diffusion resistance of the boundary layer, internal diffusion resistance of the reduced CaSO_4 layer, and resistance of the chemical reaction, respectively. Their relative magnitude varies with the nature of the solid phase particles, ambient fluid velocity, temperature, particle size, and other factors. Furthermore, this leads to the variation in the limiting link during the reduction reaction process. The relative magnitudes of the influence of the aforementioned links can be obtained from the relative magnitudes of β , $D_{AB,e}$, and k . The common reaction mechanism identification effects are listed in Table 2 [36].

Table 2. Identification of reaction mechanism in different limiting steps.

Reaction Mechanism	Increase Fluid Velocity	Apparent Activation Energy	Change the Initial Particle Size
Chemical reaction control	No impact	42–420 kJ/mol	The reaction rate is inversely proportional to r
Internal diffusion control	No impact	4.2–21 kJ/mol	The reaction rate is inversely proportional to r_0^2
External mass transfer control	Increased reaction rate	4.2–21 kJ/mol	The reaction rate is inversely proportional to r_0^n

Yan et al. [37] investigated the kinetics of the high-temperature decomposition of CaSO_4 using a shrinking nucleus model. They concluded that the SO_2 concentration of the reaction system had a significant inhibitory effect on its decomposition. The concentration of SO_2 and O_2 on the surface of the unreacted nucleus increased and decreased as the reaction progressed. The average porosity of the product layer decreased with time, which provides insight into the study of the mechanism of CaSO_4 decomposition. This is why the chemical reaction model studied in this work uses a component transport model based on the nucleation model for the simulation study of CaSO_4 reduction by gaseous sulfur in the reduction furnace.

Similar to the calcium carbonate decomposition model, the CaSO_4 decomposition model is referred to as the calcium carbonate decomposition mechanism. Khinast et al. [38] showed that both chemical reactions and mass transfer within calcium carbonate particles play a controlling role in the reaction rate. Satterfield and Feakes [39] conducted thermogravimetric studies on calcium carbonate particles of different sizes and discovered that the thermal decomposition of calcium carbonate in small particles was mainly controlled by chemical reactions. Presently, national and international studies have shown that the decomposition process of fine calcium carbonate powder particles in suspension are mainly controlled by chemical reactions. This conclusion has been affirmed by most scholars. In this study, a gas–solid reaction model based on the nucleation model is established for numerical simulation, and the main reactions in the model are as follows:



Because the reaction mechanism is controlled by a chemical reaction, its boundary and internal diffusion resistance can be neglected. Hence, Equation (9) can be simplified as:

$$t = \frac{\rho_s R_0 K [1 - (1 - f)^{1/3}]}{k(c_{A,0} - c_{A,e})(1 + K)} \quad (12)$$

where ρ_s , $c_{A,0}$, and $c_{A,e}$ are calculated based on the Fluent component transport model, R_0 is the particle size (obeying the Rosin–Rammler distribution), K is the equilibrium constant of the reaction, k is the reaction rate constant obtained from the Arrhenius equation, f is the conversion rate ($f = (n_0 - n_t)/n_0$), n_0 is the initial number of solid reactants moles, and n_t is the number of solid reactants moles at time t .

The chemical reaction kinetic data for reaction 10 were obtained from the findings in the literature [13] that the one-step reaction mechanism for the reduction of phosphogypsum by gaseous sulfur is chemically controlled, and the kinetic equation is as follows:

$$\frac{da}{dt} = 1.87 \times 10^5 \exp(-1.59 \times 10^5 / RT)(1 - \alpha) \quad (13)$$

The chemical reaction kinetic data for reaction 11 were derived from the literature [40], and the chemical reaction kinetic equation is:

$$\frac{da}{dt} = 5.2 \times 10^6 \exp(0/RT)(1 - \alpha) \quad (14)$$

The total reaction rate of the gas–solid reaction can be obtained by substituting the data in Equation (14) into (13). The particle size of the solid-phase particles and rate constant of the gas–solid reaction are introduced into the component transport model using Fluent, which accurately describes the gas–solid reaction process which is controlled by the chemical reaction.

The change in the standard molar reaction Gibbs free energy ($\Delta_r G_m$) of reaction 11 is shown in Figure 4 [41]. The direction, mode, and priority of the reaction are determined depending on whether $\Delta_r G_m$ is less than 0. The results of the thermodynamic reaction calculations show that gaseous sulfur and phosphogypsum progressed spontaneously above 1073 K, while the direct thermal decomposition reaction temperature of phosphogypsum was 1573 K. Hence, it did not decompose directly. In this reaction stage, the gaseous sulfur reduction of CaSO_4 to produce CaS is the main reaction. Compared to the occurrence of multiple side reactions in the reduction of phosphogypsum with coke, the temperature control of the sulfur gas in the pre-decomposition stage of CaSO_4 is milder, and the reaction temperature is between 1023 and 1223 K.

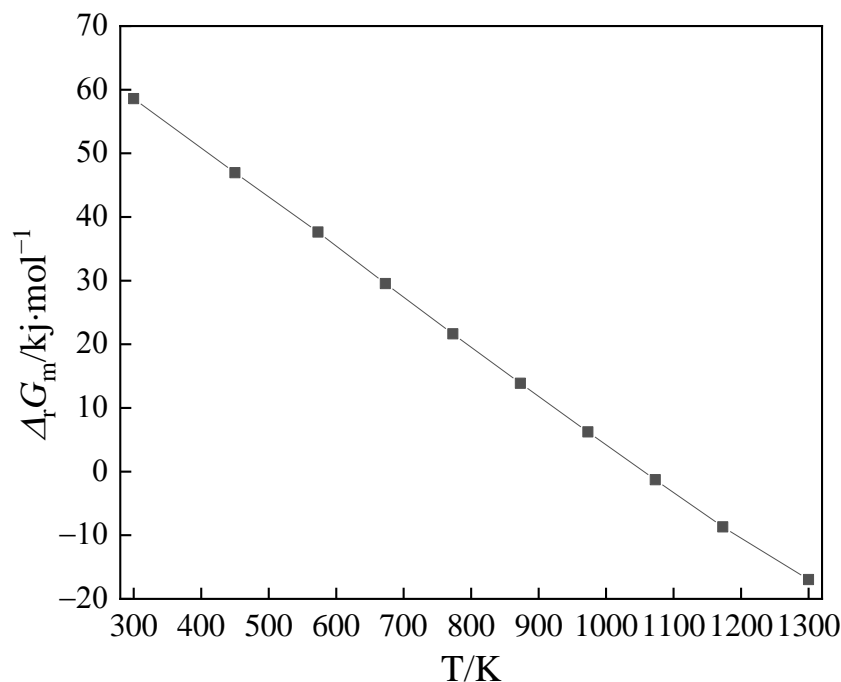


Figure 4. Gibbs free energy change of standard molar reaction of stage one ($\Delta_r G_m$).

3.3. Boundary Conditions and Numerical Solution

At room temperature, sulfur monomers existed mainly in the form of S_8 . As shown in Figure 5, with an increase in temperature, S_8 is converted to S_6 , S_4 , and S_2 . The volume fraction of S_2 in the sulfur gas system reached approximately 97% when the temperature was 1023 K. In the reduction furnace, S_2 reacted directly with CaSO_4 . Hence, the temperature of the sulfur gas inlet must not be lower than 1023 K.

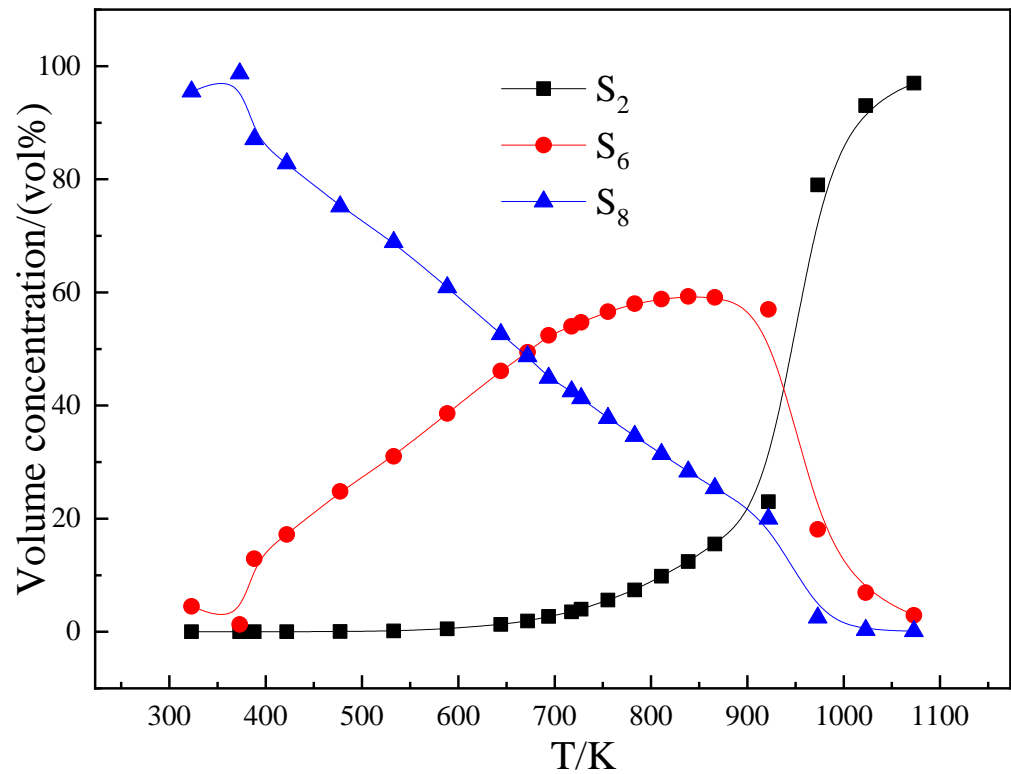


Figure 5. Volume fraction of each component in gas sulfur.

The boundary types for each part of this study are as follows: the kiln tail flue gas inlet is a velocity inlet, and the outlet and discrete phase condition are free flowing and “trapped,” respectively. Particles stop tracking when they move to the boundary interface. The raw material particles and sulfur gas inlet are mass flow rates, and the wall is a fixed non-slip. The main components of the kiln tail flue gas inlet gas are O₂, CO₂, and N₂. The O₂ and CO₂ contents were controlled at 2 and 16%, respectively. The rest were N₂. The other boundary-specific parameters are listed in Table 3. The particle size of the raw material obeyed the Rosin–Rammler distribution. The minimum, maximum, and median particle sizes were 10, 80, and 25 μm, respectively.

Table 3. Parameter setting of each boundary condition.

Boundary	Velocity/m·s ⁻¹	Mass Flow/kg·s ⁻¹	Temperature/K	DPM	Boundary Type
Inlet	20	-	1173	Escape	Velocity inlet
Sulfur gas inlet	-	0.3	1023	Escape	Mass flow inlet
Particle inlet	-	2	870	Wall-jet	Mass flow inlet
Outlet	-	-	-	Trap	Outflow

The pressure-based solver in a steady state was chosen. The SIMPLEC algorithm was used for the pressure–velocity coupling mode. The second-order windward differential format with a higher accuracy was chosen for the spatial discretization of other variables, such as the turbulent kinetic energy. The residual criterion for the energy and radiation equations was 10⁻⁵, and that for the rest of the equations was 10⁻³ to ensure that the setup parameters fulfilled the accuracy requirements of most engineering problems.

3.4. Model Validation

In this study, a tetrahedral–hexahedral hybrid grid was used for meshing the model. To exclude the influence of the grid number on the accuracy of the calculation results, the grid numbers of 60,018, 79,441, 117,732, 370,557, 487,569, 675,006, and 909,950 were selected for the calculation, and the average temperature distribution of the $X = 0$ cross-section inside the reduction furnace under seven grid numbers is shown in Figure 6. The calculation results show that the average temperature of the $X = 0$ section inside the reduction furnace is stable when the number of grids is greater than 300,000. Considering the problems related to calculating realism and resource time, this study adopted a grid number of 487,569 for subsequent numerical simulations.

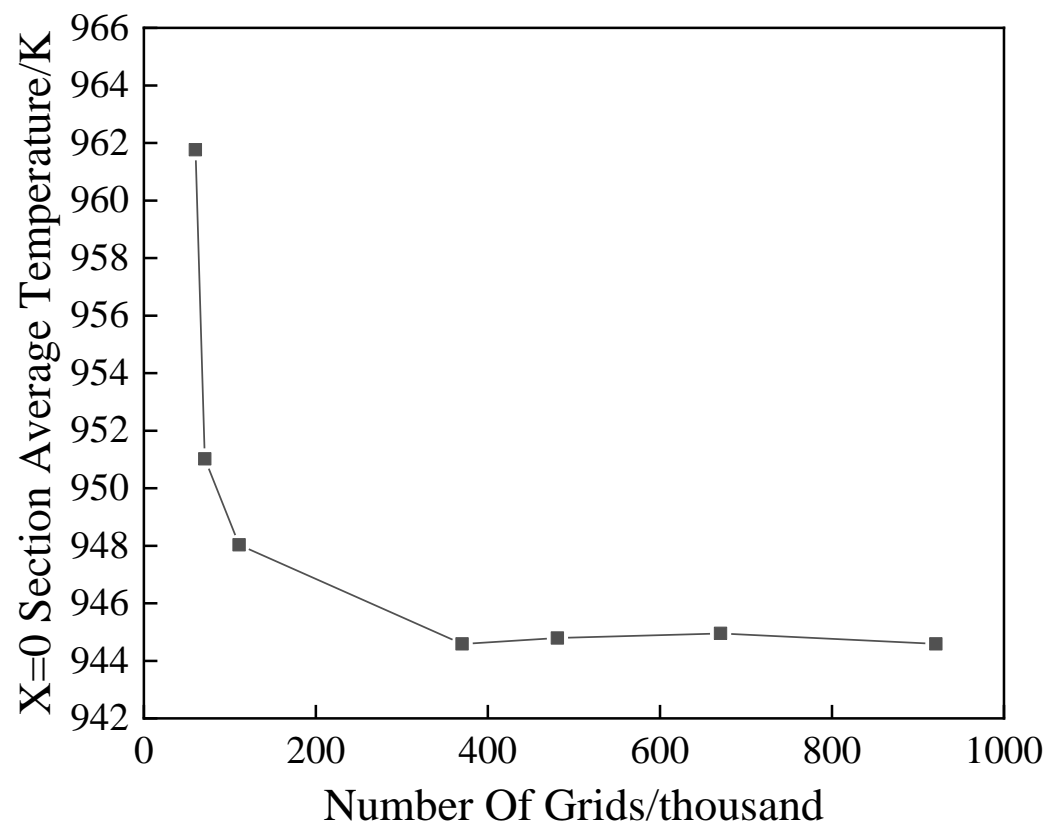


Figure 6. Grid independence verification.

Verification of the turbulence model in the reduction furnace is important. For the same structure size and grid conditions, the reduction furnace was simulated under different turbulence models, and the results are shown in Figure 7. The figure shows that, out of the four turbulence models, the calculation results of the realizable $k-\epsilon$ and Reynolds stress models are on the high side, and those of the SST $k-\epsilon$ model are closest to the test data. Therefore, the model selected for this study is confirmed to have high reliability.

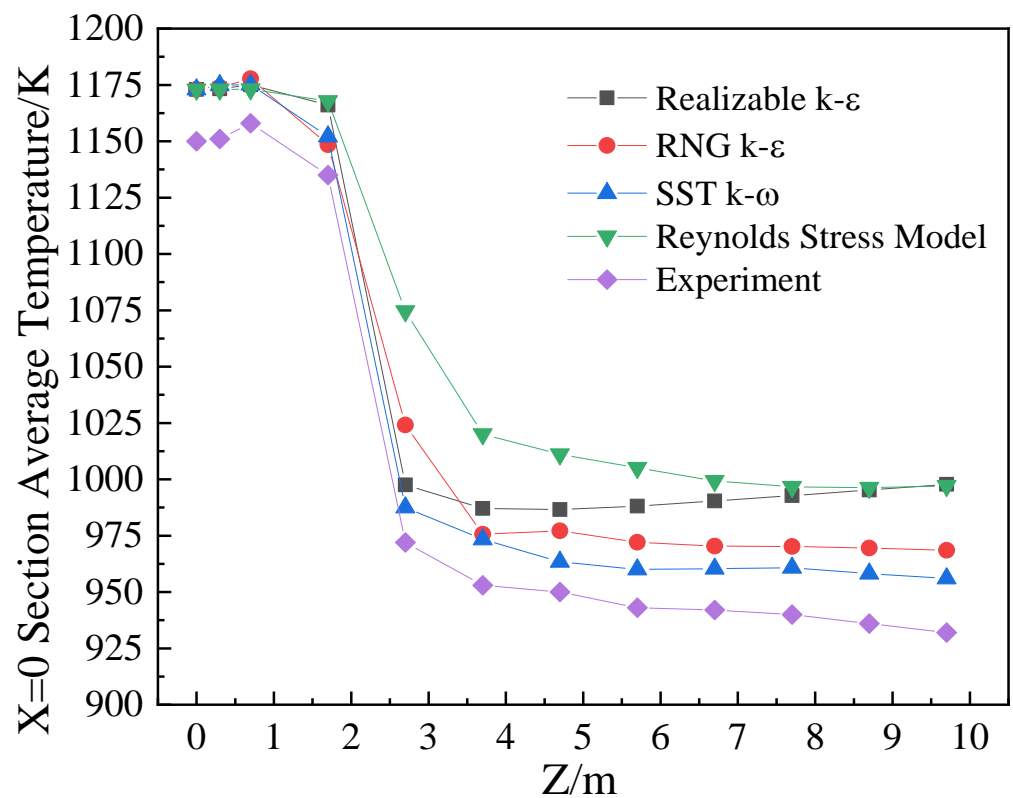


Figure 7. Model independence verification.

4. Results

4.1. Validation of Test Results

To ensure that the experimental data fulfill the requirements for deep reduction, the experiments were conducted at a molar ratio of 3.14. The flow chart of the sulfur gas reduction phosphogypsum system is shown in Figure 8, wherein the dried and broken phosphogypsum, clay, and other raw materials after fine grinding are added and homogenized in a given ratio to form raw material, which is fed into the high solid-to-gas ratio suspension preheating and pre-reduction unit. This is a multi-stage heat exchange with high-temperature flue gas from the external circulation suspension furnace. The high-temperature raw material enters the external circulation suspension furnace and completes the pre-reduction reaction with high-temperature sulfur gas between 2 and 45 s in the conveying state to form the raw material to the kiln. This controls the pre-decomposition rate of CaS by 30%. The pre-reduction reaction, the formation of raw material in the kiln, controls the phosphogypsum pre-decomposition rate of 25–30%, i.e., a CaS and CaSO₄ molar ratio of approximately 0.28:1. The raw material in the kiln flows into the rotary kiln to complete the secondary reduction ($\text{CaS} + 3\text{CaSO}_4 = 4\text{CaO} + 4\text{SO}_2$) and cement clinker sintering reaction, i.e., the high-temperature sintering of mature material into storage after grate cooler cooling. The high-temperature sulfurous flue gas from the preheating system is purified by dust removal. It is further converted and absorbed to produce sulfuric acid.

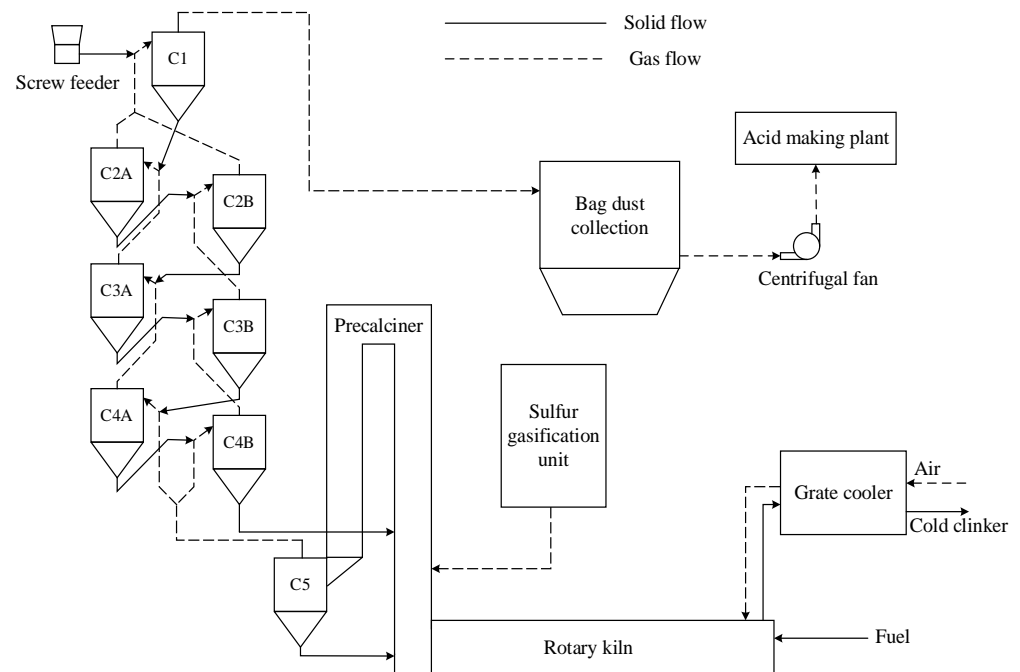


Figure 8. Process flow diagram of sulfur gas reduction phosphogypsum system.

The solid sulfur is liquefied in the molten sulfur tank, with the temperature within 393–433 K. The coarser liquid sulfur is formed by melting. The liquefied sulfur in this temperature range has the smallest viscosity and best fluidity. The fine filtered sulfur liquid is pumped into the sulfur gasification unit and heated to 723–823 K. The liquid sulfur is atomized by the atomization nozzle and gasified rapidly. It is heated to 773–1173 K by the medium frequency heating furnace to ensure the highest diatomic sulfur content of the ejected sulfur gas. The high-temperature sulfur gas is sent to the bottom of the reduction furnace by the venturi inducer. It reacts with the raw material particles entering the reduction furnace upon convergence with the flue gas at the end of the kiln between 1173 and 1273 K. The reduction atmosphere and temperature in the reduction furnace can be controlled by adjusting the amount of raw material entering the reduction furnace and sulfur gasifier discharge. Since the sulfur gasification process is fast and complete, the amount of sulfur in the reaction system can be controlled by metering liquid sulfur and fast gasification.

The reliability of the simulation results was verified by measuring the real-time temperature of each section of the reduction furnace and decomposition rate of the material outside the reduction furnace. K-type thermocouples were used to monitor the temperature changes in real time at the bottom, middle, and top of the reduction furnace. The real-time temperature signals collected by the thermocouples were transmitted to the central control display screen simultaneously. The reduction samples from the reduction furnace were removed, and the CaSO_4 and CaS contents were determined using the iodine measurement method. The decomposition rate of the raw material exported from the reduction furnace was calculated using the following equation:

$$\alpha = \frac{Mf_{\text{CaS}}}{Mf_{\text{CaS}} + Mf_{\text{CaSO}_4}} \quad (15)$$

A comparison between the measured and calculated data is presented in Table 4.

Table 4. Comparison between calculated results and measured data.

Data	Decomposition Rate/%	Calciner Temperature/K				Error/%	
		Bottom	Middle	Top	Average	Decomposition Rate	Average Temperature
Simulation calculation	21.19	1173	991	982	1048.67	8.07	3.85
Experimental	22.90	1150	943	932	1008.33		

According to the data in Table 4, the average temperature in the reduction furnace obtained from the simulation was 1048.67 K, the raw material decomposition rate was 21.19%, the actual average temperature of the reduction furnace measured under working conditions was 1008.33 K, the raw material decomposition rate was 22.90%, and the calculation error margin of the reduction furnace temperature and raw material decomposition rate were 3.85 and 8.07%, respectively. The reason for the high numerical simulation temperature results is that the wall boundary of the reduction furnace was assumed to be non-slip with no energy loss, heat transfer between the gas and solid phases and the wall was not fully considered, and the reaction between the CO generated in the rotary kiln and CaSO₄ after entering the reduction furnace was ignored in the simulation process. The feasibility of the sulfur gas reduction phosphogypsum and accuracy of the numerical calculation processes were demonstrated through a combination of numerical simulations and experimental verification.

4.2. Effect of $n(\text{CaSO}_4)/n(\text{S}_2)$ on the Decomposition Rate

Figure 9 shows the flow diagram of each phase in the reduction furnace at different $n(\text{CaSO}_4)/n(\text{S}_2)$. As $n(\text{CaSO}_4)/n(\text{S}_2)$ increases, the initial height of the CaSO₄ particles in contact with gaseous sulfur decreases. This proves that $n(\text{CaSO}_4)/n(\text{S}_2)$ can affect the efficiency of the gas–solid reaction. Under the low $n(\text{CaSO}_4)/n(\text{S}_2)$ condition, calcium sulfate particles with a low mass flow rate are incident on the reduction furnace and move rapidly upward propelled by the high-speed kiln tail flue gas. This results in their concentration on the right side of the middle and upper sections of the reduction furnace, with a small reflux zone appearing on the left side.

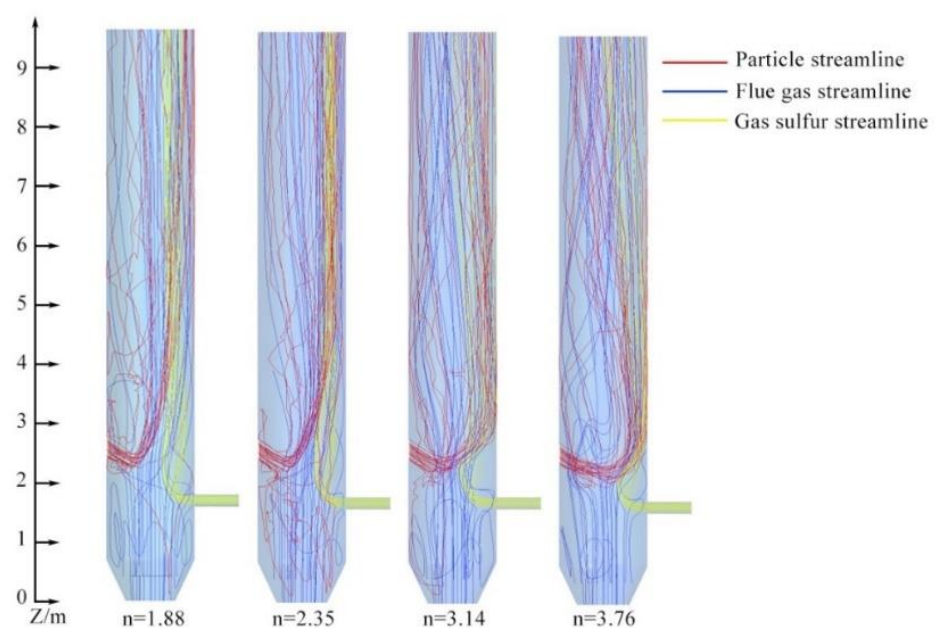
**Figure 9.** Flow diagram in reduction furnace under different $n(\text{CaSO}_4)/n(\text{S}_2)$.

Figure 10 shows the average molar fraction curves of the solid phase for each cross-section in the Z-axis. Here, the increasing trend of CaS as a product of CaSO₄ raw material particle reduction is slightly ahead of the decreasing trend of CaSO₄. This is mainly owing to the small proportion of raw material particles entering the reduction furnace while moving to the bottom of the reduction furnace under the action of the reflux vortex at the lower wall of the reduction furnace and later moving upward. Simultaneously, the content of the raw material particles entering the reduction furnace under $n = 3.14$ decreases abruptly, while that in CaS increases. This shows that the raw material particles can react with gaseous sulfur rapidly after entering the reduction furnace again under such condition and increase the overall reaction rate.

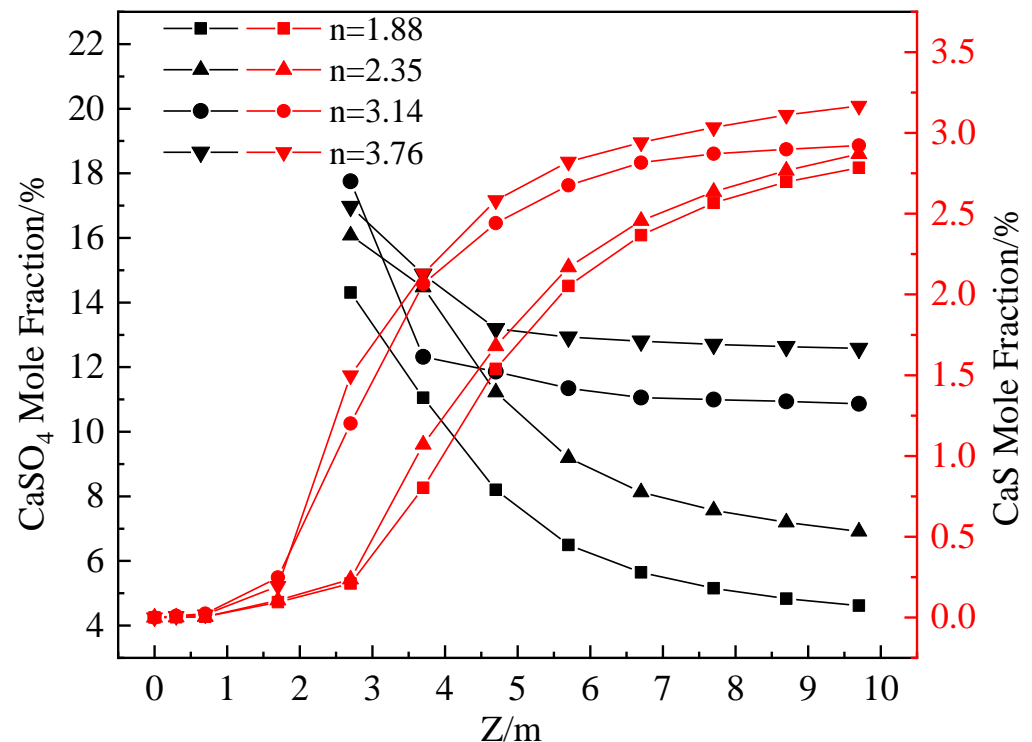


Figure 10. Curve of average mole fraction of solid phase at various sections along the Z-axis of $n(\text{CaSO}_4)/n(\text{S}_2)$ conditions.

The decomposition rate of CaSO₄ under different $n(\text{CaSO}_4)/n(\text{S}_2)$ conditions was obtained by combining the results of several sets of simulations, as shown in Figure 11. The decomposition rate of CaSO₄ was inversely proportional to $n(\text{CaSO}_4)/n(\text{S}_2)$. The reaction mechanism is controlled by the chemical reaction. As $n(\text{CaSO}_4)/n(\text{S}_2)$ increases, the molar fraction of CaSO₄ in the reaction system increases the amount of S₂ consumed and continues to. This leads to a continuous decrease in the molar fraction of S₂ in the reaction system until it is consumed, thereby causing the reaction rate to gradually decrease. The decomposition rate of CaSO₄ must be controlled within the range of 20–25% to ensure that the discharged material fulfills the deep reduction requirements. Hence, $n(\text{CaSO}_4)/n(\text{S}_2)$ must be controlled within 3.0–3.5.

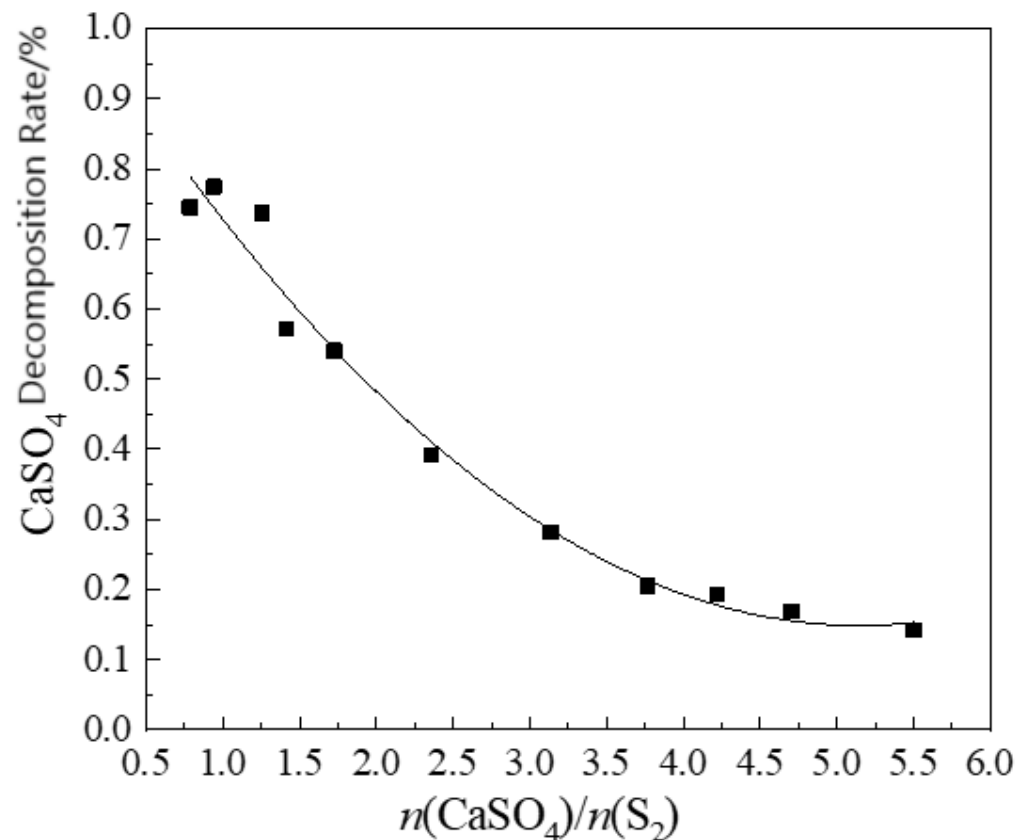


Figure 11. CaSO_4 decomposition rate curve under different $n(\text{CaSO}_4)/n(\text{S}_2)$ conditions.

4.3. Effect of Particle Residence Time on Reduction Furnace Performance

Figure 12 shows the velocity vector diagrams of the four planes which correspond with different maximum residence times of the particles in the reduction furnace. These were obtained from the sulfur gas and raw material particle inlet planes, middle of the reduction furnace, and upper flat push flow region of the reduction furnace. The reflux at planes 1 and 3 under the $t = 4.83$ s condition is more evident. However, there is a small reflux area at the opposite wall of the raw material pellet inlet of the reduction furnace in plane 2 under $t = 5.19$ s and $t = 4.83$ s conditions. The high-speed area is concentrated at the right side of the plane. A longer residence time leads to a more stable flow field trend at the upper part of the reduction furnace (plane 4), thereby causing the gas–solid flow pattern to gradually change to the advection flow.

Figure 13 shows a graph of the average molar fraction of the solid phase at each cross-section of the particles in the reduction furnace with different maximum residence times along the Z-axis. The graph of the molar fraction at the CaSO_4 inlet cross-section is relatively larger under the $t = 7.08$ s condition, while the molar fraction of CaS increases relatively fast under this condition. This can be attributed to the fact that the proportion of raw material particles entering the reflux area at the lower wall of the reduction furnace is higher under this condition than under others. This leads to an increase in the content of CaS as a product of the CaSO_4 raw material particle reduction, which slightly exceeds the decreasing trend of CaSO_4 .

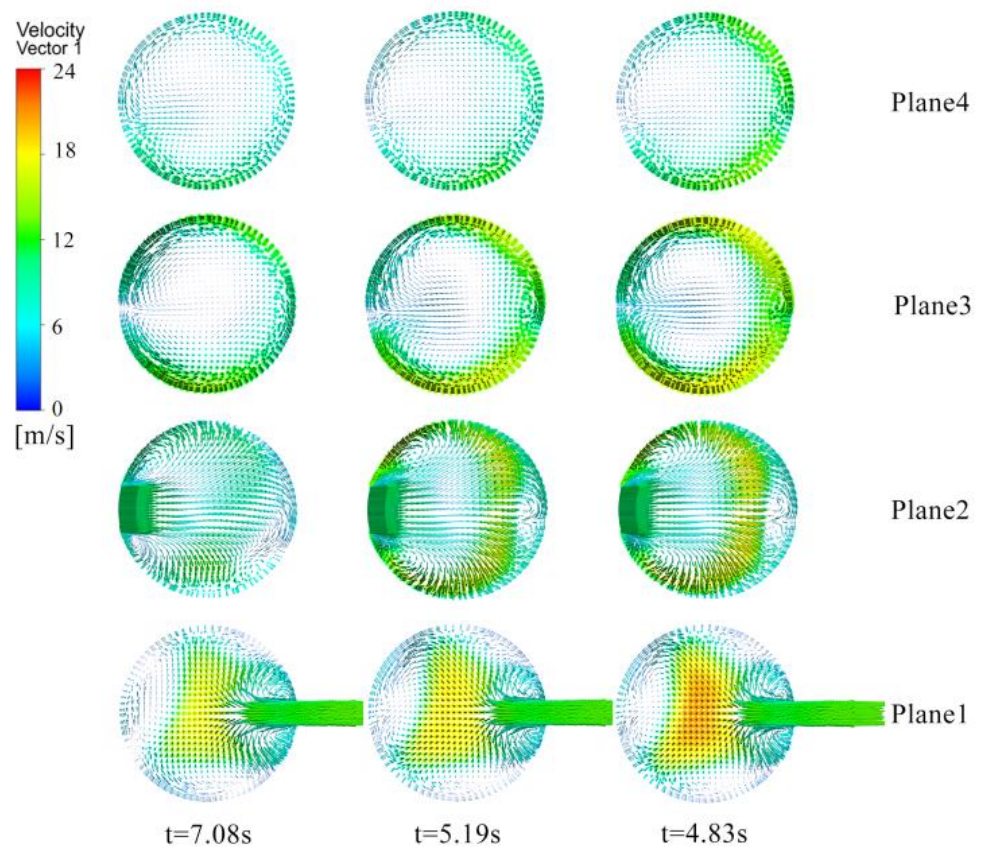


Figure 12. Velocity vector diagram of Z-axis sections under different particle residence time conditions.

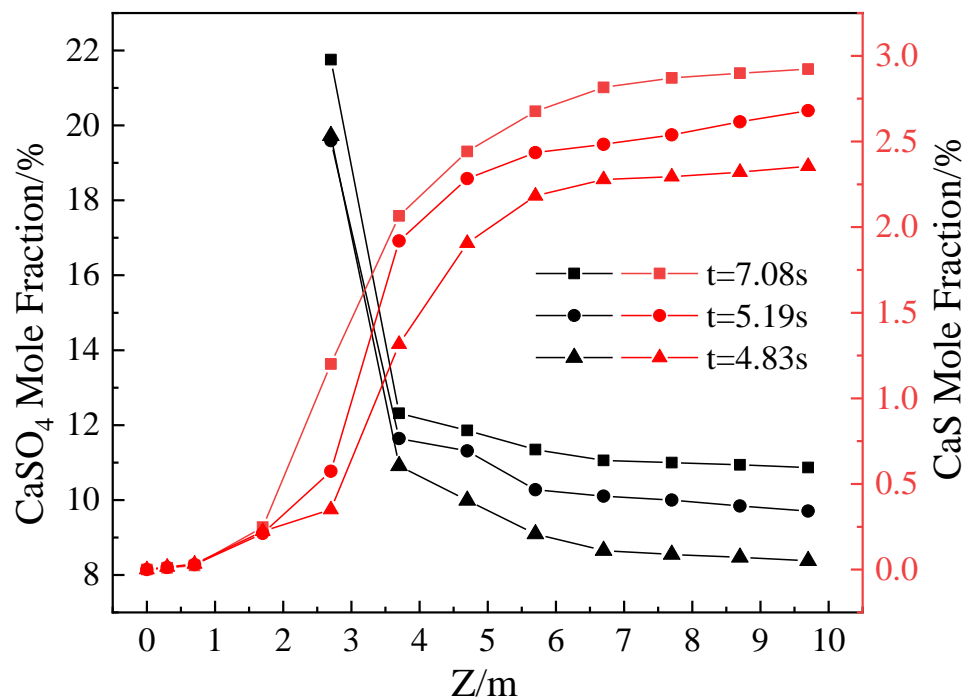


Figure 13. Curve chart of average molar fraction of solid phase at each section of Z-axis for different particle retention times.

The decomposition rate of CaSO_4 under different particle residence time conditions was analyzed using multiple sets of simulation test results, as shown in Figure 14. This shows that the decomposition rate of CaSO_4 in the reduction furnace is proportional to the particle residence time. Here, the decomposition rate of CaSO_4 gradually increases with an increase in the particle residence time. Owing to the uneven particle size distribution of the raw material particles in the reduction furnace, the specific surface area of the raw material particles with larger particle sizes at a similar residence time was relatively small, and the rate of heat absorption in the furnace was relatively slow. This resulted in a relatively low decomposition rate of CaSO_4 . Generally, under a constant particle residence time condition, the solution is to increase the temperature in the reduction furnace. By increasing the particle residence time, the reaction rate of coarse particles can be improved, and the temperature control of the reduction furnace appropriately reduced. This further reduces the temperature of the preheater and corresponding enrichment of harmful ingredients. Furthermore, the crusting in the system is reduced, which is beneficial for the safe operation of the preheater system.

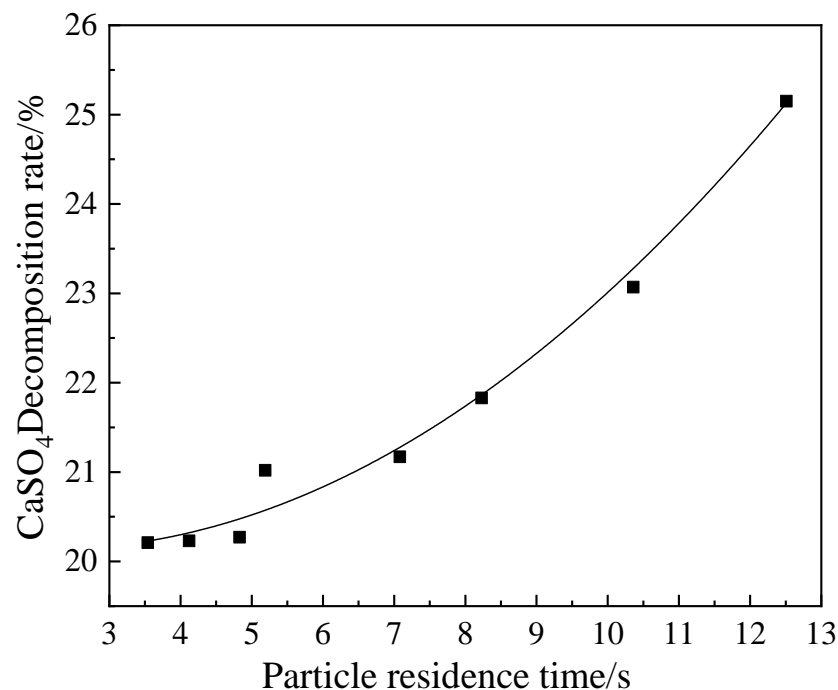


Figure 14. Curve of CaSO_4 decomposition rate with different particle retention times.

4.4. Effect of Kiln Tail Flue Gas Temperature on Reduction Furnace Performance

In Figures 15 and 16, the molar distribution of the gas–solid phase components of the reduction furnace correspond with the law. With an increase in the kiln tail flue gas temperature, the molar fraction of CaSO_4 , CaS , and SO_2 in each section of the reduction furnace gradually increases, while that of O_2 and N_2 in the furnace gradually decreases, thereby showing that an increase in the kiln tail flue gas temperature can effectively increase the chemical reaction rate. This will further improve the decomposition rate of CaSO_4 and increase the content of SO_2 in the furnace. This is very beneficial to the subsequent SO_2 conversion and absorption of sulfuric acid, thereby increasing the system's production capacity.

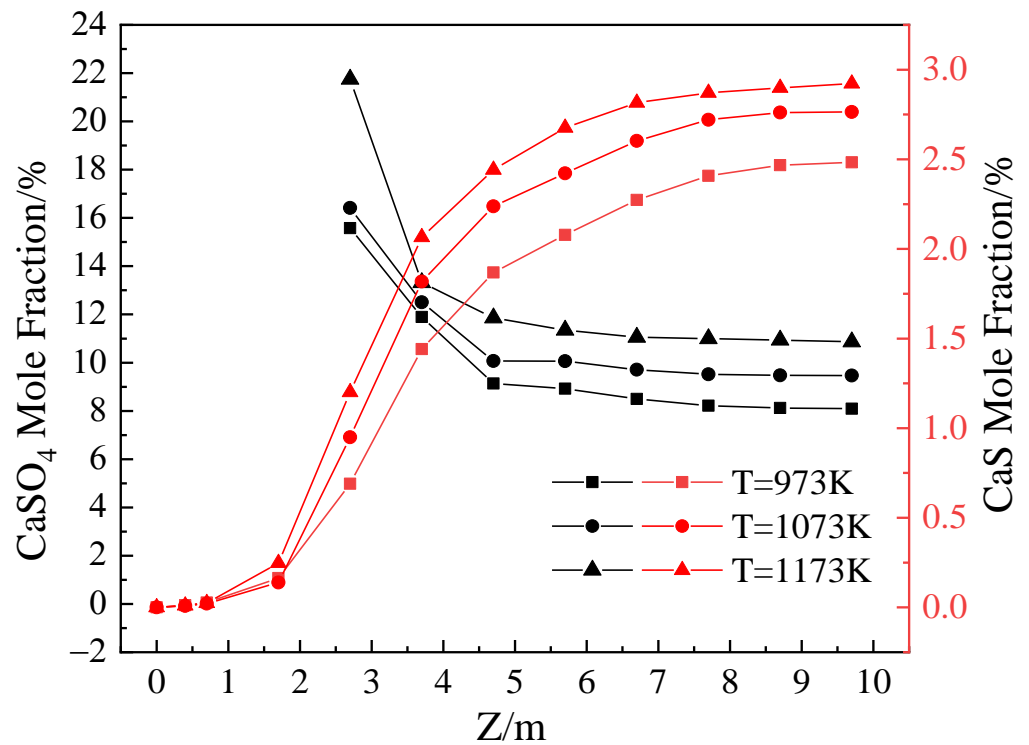


Figure 15. Curve chart of average molar fraction of solid phase at each section in the Z-axis at different flue gas temperatures.

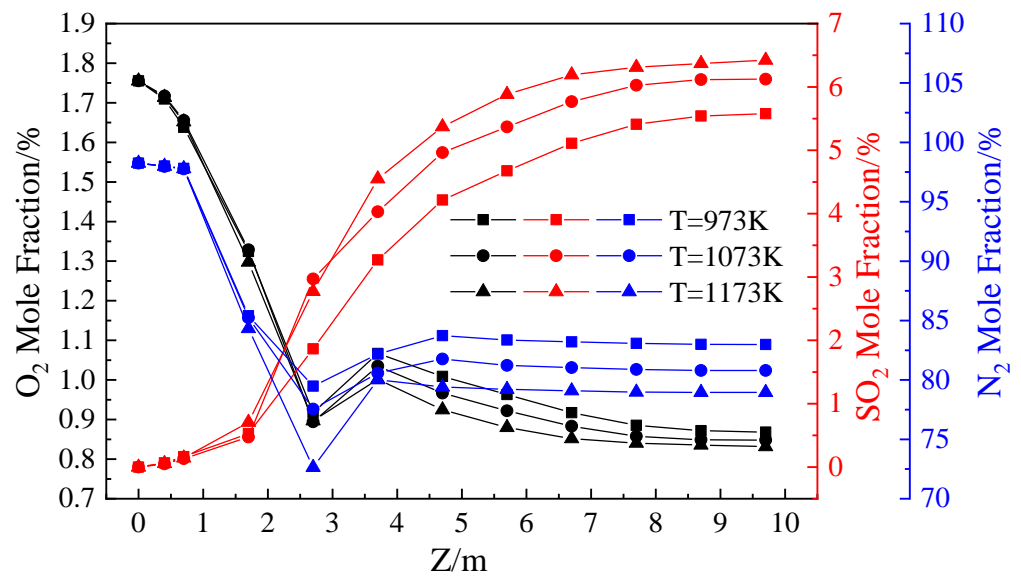


Figure 16. Curve of average molar fraction of gas phase at each section in the Z-axis of different flue gas temperatures.

Figure 17 shows a cloud plot of the temperature distribution of the X = 0 section and each section of the Z-axis in the reduction furnace at different kiln tail flue gas temperatures. Figure 18 shows a plot of the temperature distribution of each section of the Z-axis in the reduction furnace at different kiln tail flue gas temperatures. From the figure, the change in the kiln tail flue gas temperature leads to a change in the ambient temperature inside the reduction furnace, which affects the thermal efficiency of the entire reaction system. When the kiln tail flue gas temperature is low, the low-temperature area on the right side of the middle of the reduction furnace is more evident, while the temperature distribution at

the top is not uniform. When the kiln tail flue gas temperature is high, a high-temperature area develops on the right side of the bottom of the reduction furnace. This results in an increasing trend of the Z-axis section temperature at the bottom of the reduction furnace. This is owing to the small portion of sulfur gas entering this reflux area to burn exotherm. Generally, increasing the kiln tail flue gas temperature can improve the uneven temperature distribution at the upper part of the reduction furnace while increasing the reaction rate.

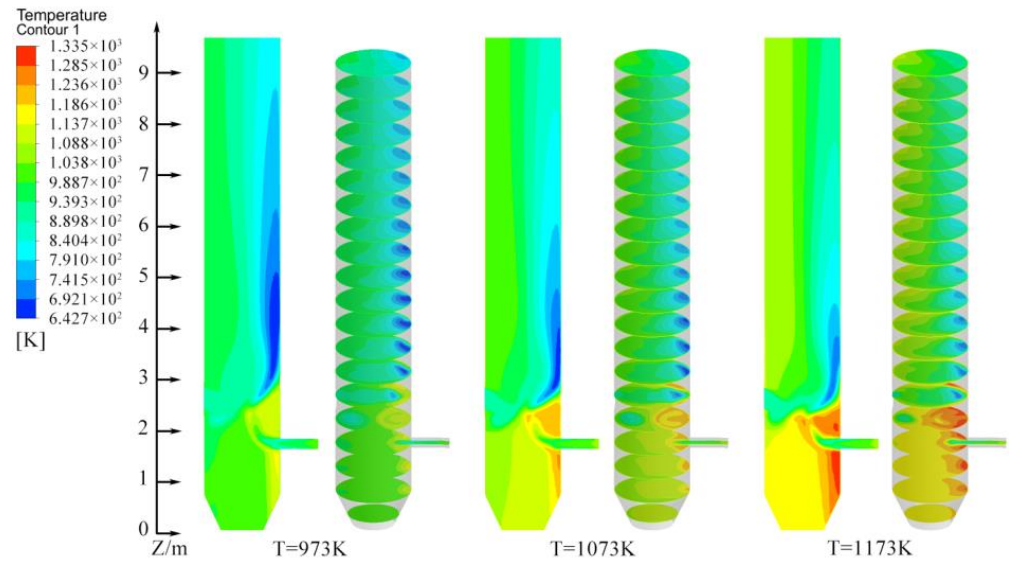


Figure 17. Cloud chart of temperature distribution of sections with different flue gas temperatures $X = 0$ and Z -axis.

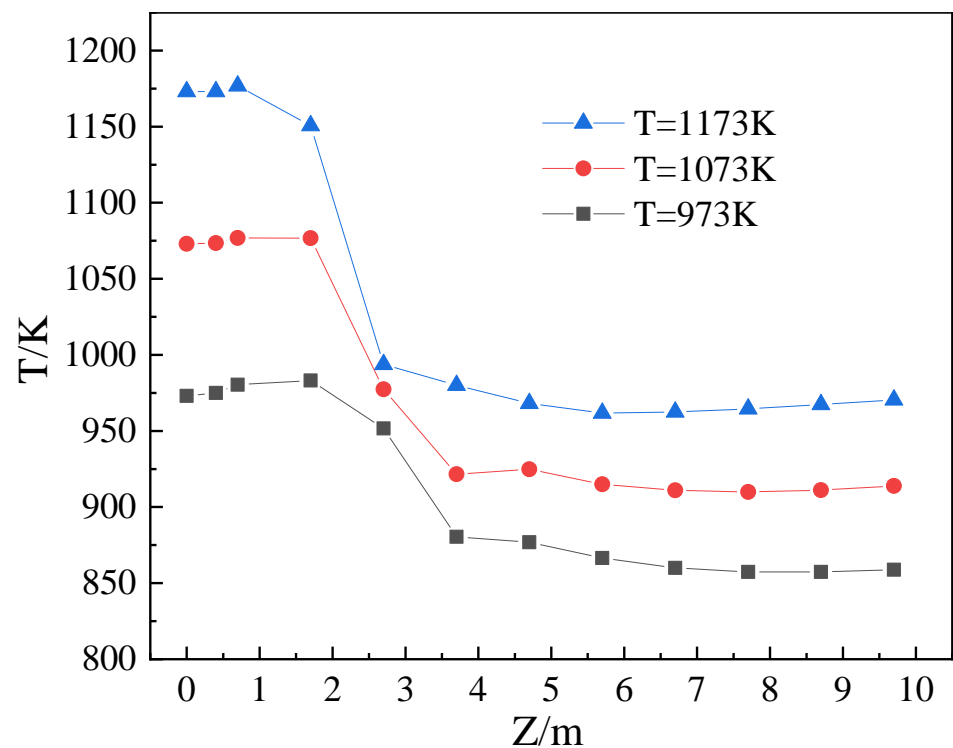


Figure 18. Temperature distribution curve of Z -axis sections of reductor with different flue gas temperatures.

4.5. Response Surface Analysis of Reduction Furnace Operating Parameters

According to the BBD experimental design, a three-factor, three-level response surface analysis test was designed based on a single-factor test. $n(\text{CaSO}_4)/n(\text{S}_2)$, particle residence time, and kiln tail flue gas temperature were the three independent variables. The raw material CaSO_4 decomposition rate was the response value. The experimental factors and levels are shown in Table 5.

Table 5. Experimental factors and levels.

Factor		Level		
		−1	0	1
$n(\text{CaSO}_4)/n(\text{S}_2)$	x_1	2.5	3.1	3.7
Particle residence time/s	x_2	5	7	9
Flue gas temperature/K	x_3	1073	1173	1273

The experimental design and results are presented in Table 6. Multiple regression analysis and binomial fitting were performed for each factor and response value to obtain the CaSO_4 decomposition rate response surface model equation, as expressed as follows:

$$Y = 21.50 - 3.85x_1 + 0.5725x_2 + 0.7213x_3 + 0.9175x_1x_2 + 0.1150x_1x_3 - 0.1325x_2x_3 + 0.7490x_1^2 + 0.7665x_2^2 - 0.0890x_3^2 \quad (16)$$

Table 6. Experimental design and results.

Experiment Number	x_1	x_2	x_3	Y
1	−1	−1	0	26.66%
2	1	−1	0	17.73%
3	−1	1	0	26.47%
4	1	1	0	21.21%
5	−1	0	−1	25.96%
6	1	0	−1	17.42%
7	−1	0	1	27.03%
8	1	0	1	18.95%
9	0	−1	−1	21.11%
10	0	1	−1	22.02%
11	0	−1	1	22.96%
12	0	1	1	23.34%
13	0	0	0	21.88%
14	0	0	0	21.25%
15	0	0	0	21.84%
16	0	0	0	21.52%
17	0	0	0	21.02%

The ANOVA of the second-order model is shown in Table 7, and the p -value of the significance test of the model is less than 0.0001. This shows that the model was statistically significant. The difference between the modified decision coefficient $R^2(\text{adj})$ and prediction coefficient $R^2(\text{pred})$ is less than 0.2, showing that the model is fit for use and can be used for the preliminary analysis and prediction of the process. In Table 7, the p -values of all the primary terms of the independent variables (x_1, x_2, x_3) are less than 0.05, and all three single factors are significant. This shows that $n(\text{CaSO}_4)/n(\text{S}_2)$ and flue gas temperature had the greatest effect on the CaSO_4 decomposition rate of the reduction furnace, followed by the

particle residence time. The P-values of the secondary terms of the independent variables ($x_1 x_2$, x_1^2 , x_2^2) were all significant factors. The p -values were less than 0.05, revealing that the combined effect of $n(\text{CaSO}_4)/n(\text{S}_2)$ and particle residence time had a greater influence on the CaSO_4 decomposition rate of the reduction furnace.

Table 7. Analysis of variance of the second-order model.

Source	Sum of Squares	df	Mean Square	F-Value	p -Value	Significance
Model	134.16	9	14.91	56.96	<0.0001	significant
x_1	118.66	1	118.66	453.38	<0.0001	
x_2	2.62	1	2.62	10.02	0.0158	
x_3	4.16	1	4.16	15.90	0.0053	
$x_1 x_2$	3.37	1	3.37	12.87	0.0089	
$x_1 x_3$	0.0529	1	0.0529	0.2021	0.6666	
$x_2 x_3$	0.0702	1	0.0702	0.2683	0.6204	
x_1^2	2.36	1	2.36	9.03	0.0198	
x_2^2	2.47	1	2.47	9.45	0.0180	
x_3^2	0.0334	1	0.0334	0.1274	0.7316	
Residual	1.83	7	26.17			
Lack of fit	1.28	3	0.4262	3.08	0.1527	not significant
Pure error	0.5533	4	0.1383			
Cor Total	135.99	16				

$R^2 = 0.9865$, $R^2(\text{adj}) = 0.9692$, $R^2(\text{pred}) = 0.8432$

A three-dimensional CaSO_4 decomposition rate response surface was established based on the regression equation which clearly showed the interaction of the factors. Figure 19 shows the interaction between $n(\text{CaSO}_4)/n(\text{S}_2)$ and particle residence time, which has the greatest effect on the CaSO_4 decomposition rate. The CaSO_4 decomposition rate increases significantly with a decrease in $n(\text{CaSO}_4)/n(\text{S}_2)$ and an increase in the particle residence time in a given range. Figure 20 shows the interaction between $n(\text{CaSO}_4)/n(\text{S}_2)$ and the flue gas temperature, wherein the CaSO_4 decomposition rate increases with decreasing $n(\text{CaSO}_4)/n(\text{S}_2)$ and increasing flue gas temperature. Figure 21 shows the interaction between the particle residence time and flue gas temperature. Here, the CaSO_4 decomposition rate increases with an increase in particle residence time and flue gas temperature. The response surface curve of the effect of $n(\text{CaSO}_4)/n(\text{S}_2)$ on the CaSO_4 decomposition rate is slightly steeper, and the corresponding contour lines are more intense, as shown in Figure 19. This reveals that the effect of $n(\text{CaSO}_4)/n(\text{S}_2)$ on the CaSO_4 decomposition rate is more significant than the particle residence time. Similarly, it can be concluded that the effect of $n(\text{CaSO}_4)/n(\text{S}_2)$ on the CaSO_4 decomposition rate is more significant than that of the flue gas temperature (Figure 20). In Figure 21, the effect of the particle residence time on the CaSO_4 decomposition rate is more significant than that of the flue gas temperature. Based on the above three response surface plots, it can be concluded that among the interactions of different factors, $n(\text{CaSO}_4)/n(\text{S}_2)$ had the most significant effect on the CaSO_4 decomposition rate, followed by particle residence time. This is attributable to the fact that $n(\text{CaSO}_4)/n(\text{S}_2)$ in the reduction furnace was mainly determined by the raw material ratio, which determined the decomposition rate of raw material to a great extent. This is the most important factor that affects the decomposition rate of raw material out of the reduction furnace and nature of the material exiting the reduction furnace.

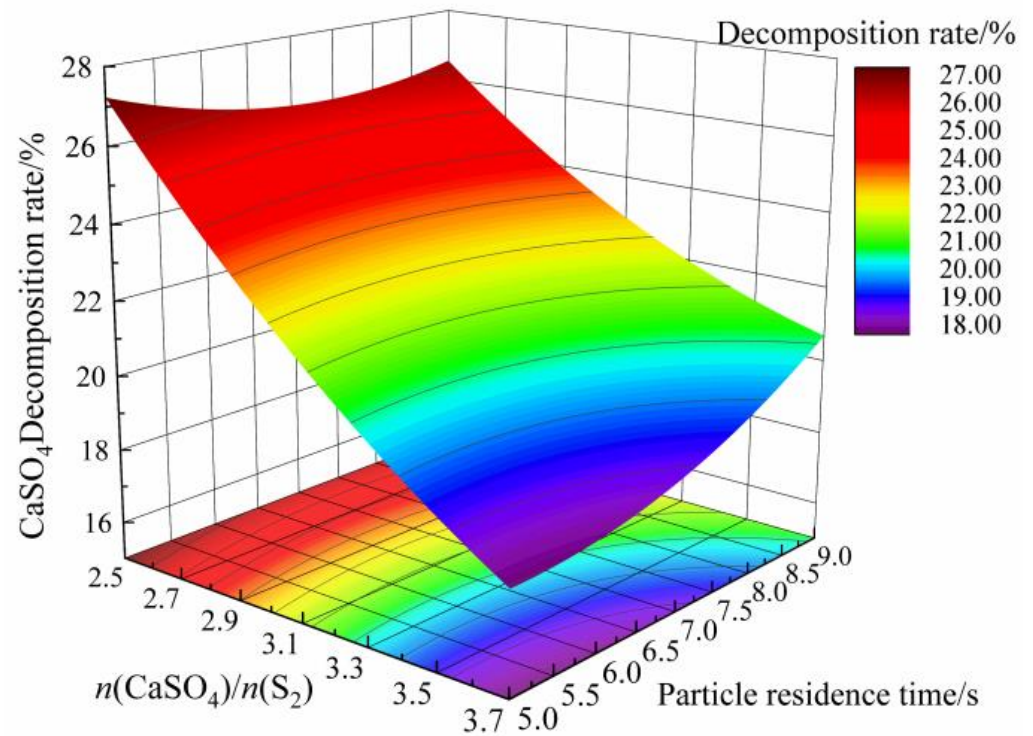


Figure 19. Effect of $n(\text{CaSO}_4)/n(\text{S}_2)$ and particle residence time on decomposition rate of CaSO_4 .

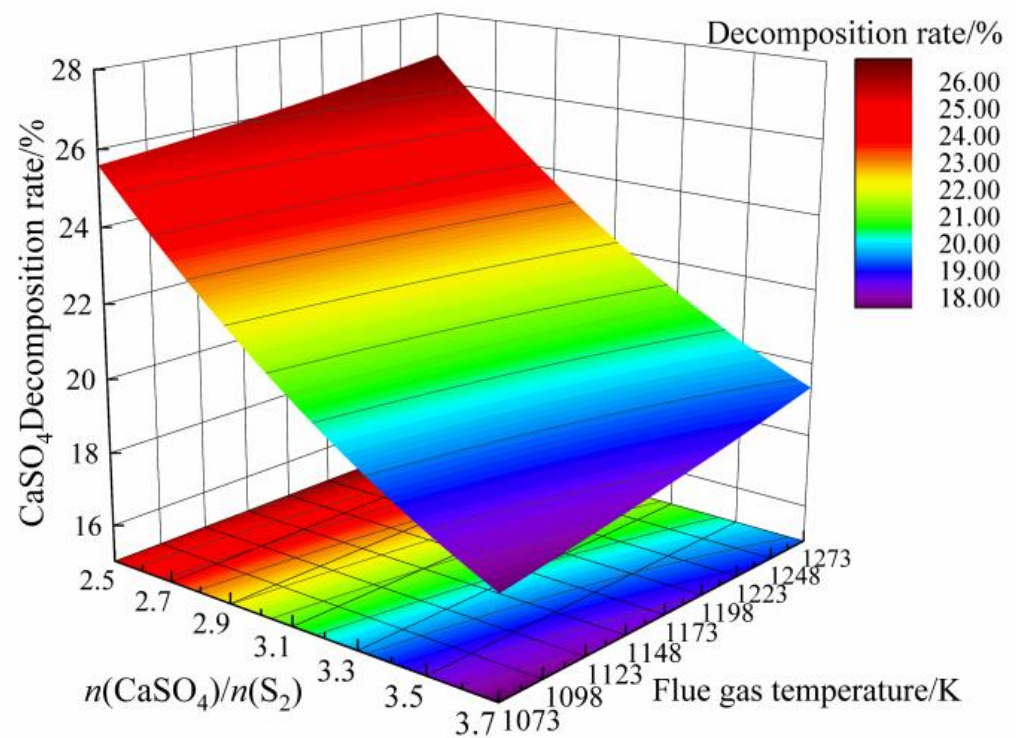


Figure 20. Effect of $n(\text{CaSO}_4)/n(\text{S}_2)$ and flue gas temperature on decomposition rate of CaSO_4 .

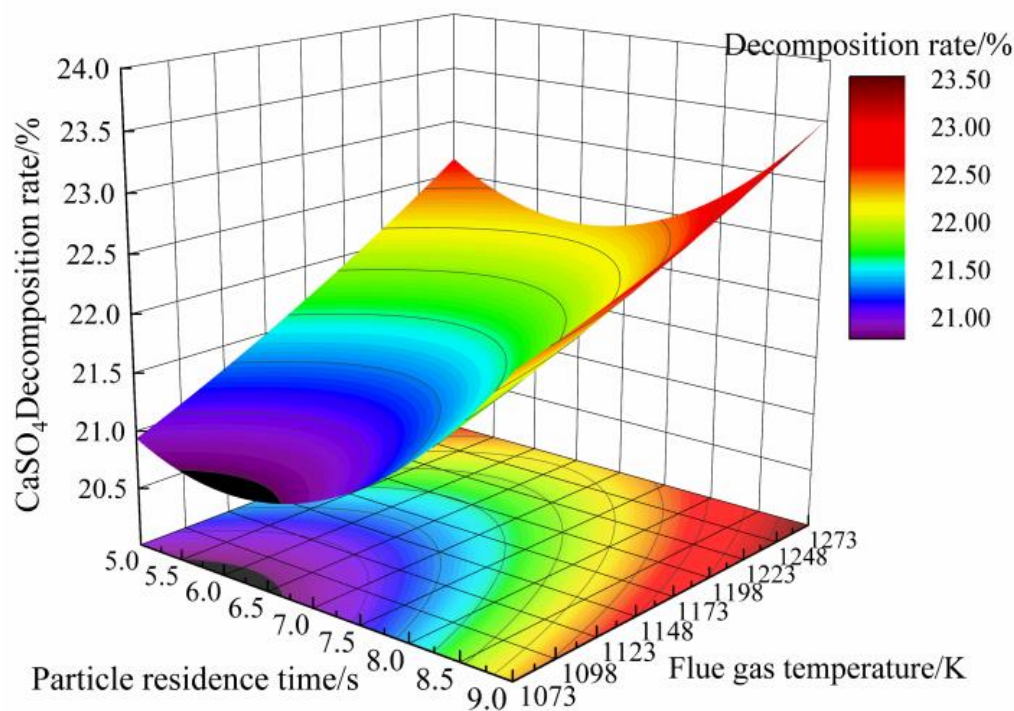


Figure 21. Effect of particle residence time and flue gas temperature on CaSO₄ decomposition rate.

The parameter variables were optimized after the optimal process range was determined by three-dimensional response surface analysis. The CaSO₄ range was increased from 23% to 27%, and the process parameters were optimized under this condition to finally arrive at the optimal parameter combination.

Table 8 shows a comparison of the process parameters and CaSO₄ decomposition rate before optimization and after optimization. $n(\text{CaSO}_4)/n(\text{S}_2)$ is 3.04, and the subject residence time and flue gas temperature are controlled at 8.90 s and 1265.39 K, respectively. Under this condition, the response surface predicts that the CaSO₄ decomposition rate is 23.64% and the experimentally calculated CaSO₄ decomposition rate is 23.24%, with a relative error of 1.69%. This comparison shows that the CaSO₄ decomposition rate reached 23.24% after optimization, which was 9.64% higher than that before optimization. The experiments proved the accuracy and feasibility of the optimization model.

Table 8. Process parameters before and after optimization.

Optimization	$n(\text{CaSO}_4)/n(\text{S}_2)$	Particle Residence time/s	Flue Gas Temperature/K	Decomposition Rate/%		Error/%
				Forecast	Experiment	
Before	3.1	7	1173	-	21.19	-
After	3.04	8.90	1265.39	23.64	23.24	1.69

5. Discussion

This paper innovatively applies the numerical simulation method to the gas sulfur reduction of phosphogypsum in a dilute phase fluidized reduction furnace. Compared with the fixed bed, moving bed, and dense phase fluidized bed, the advantages of the test method in this paper are the void ratio in the dilute phase transport bed is large, the particle volume fraction is extremely low, the particle surface is completely submerged in the gas, the particles can be somewhat preferentially fully dispersed in the gas, and the phenomenon of adhesion and agglomeration into the flocculation between particles is rare. In the dilute phase transport system, the gas phase and particle turbulence are fully developed, increasing the Reynolds coefficient and reducing the thickness of the

temperature boundary (surface layer) and mass transfer boundary layers (surface layer). The temperature and concentration gradients become larger, increasing the transfer power. The heat and mass transfer rates are greatly enhanced.

The results of the simulation reported in this study are compared with the results of other studies as shown in Table 9. The results of the literature [12,13] showed a one-stage reaction temperature of 993 K, a reaction residence time of 60 min for the phosphogypsum, and that the reaction products could reach the two-stage material ratios. In contrast, the dilute phase fluidized reduction furnace considered in this study was able to reduce the phosphogypsum to meet the subsequent process requirements at a reaction temperature of 1265.39 K and a residence time controlled within 10 s. The advantage of this study is that the residence time is significantly reduced, and the reaction rate constant is increased by more than 80 times. In this study, only the influence of the reduction furnace operating parameters on its performance is studied, without considering the influence of the reduction furnace structural parameters. Meanwhile, the set of optimal values obtained by the response surface analysis method is difficult to precisely control under actual operating conditions; therefore, the correction of the parameter fluctuations during actual operation should be considered in the subsequent study to ensure the validity of the simulation test.

Table 9. Comparison of the results of this study with other research results.

Target	Reaction Temperature	Particle Residence Time
Research results [12,13]	993 K	60 min
Results of this study	1265.39 K	8.9 s

6. Conclusions

A numerical simulation study of the reduction furnace of the main plant in acid production from phosphogypsum by sulfur gas reduction was conducted using the CFD method. The coupled process temperature and component fields of turbulence and chemical reactions in the reduction furnace were analyzed to obtain specific physicochemical change processes of sulfur gas and raw material particles in the reduction furnace.

A gas–solid chemical reaction model for the reduction of CaSO_4 by sulfur gas in a reduction furnace was established, and the feasibility of the sulfur gas reduction process of phosphogypsum and accuracy of the numerical calculation process were demonstrated through a combination of numerical simulations and experimental verification.

The inlet $n(\text{CaSO}_4)/n(\text{S}_2)$ ratio had a certain degree of influence on the flow field, temperature, and decomposition rate of CaSO_4 in the reduction furnace. The high inlet $n(\text{CaSO}_4)/n(\text{S}_2)$ stabilized the gas–solid phase flow and temperature fields in the furnace, although it had a negative influence on the decomposition rate of CaSO_4 .

Increasing the particle residence time mainly affected the flow field distribution in the upper part of the reduction furnace. The difference in the kiln tail flue gas flow rate projected its motion trajectory to the right side of the reduction furnace upon intersection with the sulfur gas and raw material particles. As the particle residence time increased, the flow field in the upper part of the furnace increasingly stabilized and the CaSO_4 decomposition rate gradually increased. By increasing the particle residence time, the overall temperature in the reduction furnace gradually decreased. Simultaneously, the reaction efficiency of the raw material particles and sulfur gas were improved.

The change in the kiln tail flue gas temperature had little effect on the gas–solid two-phase flow field in the reduction furnace. However, it had a greater effect on the ambient temperature and CaSO_4 decomposition rate in the reduction furnace. Increasing the kiln tail flue gas temperature will lead to an increase in the ambient temperature, which is conducive to improving the equilibrium yield of the heat absorption reaction. It can also accelerate the chemical reaction rate between the sulfur and CaSO_4 gases in the furnace and improve the uneven temperature distribution in the upper part of the reduction furnace.

The selected process parameters $n(\text{CaSO}_4)/n(\text{S}_2)$, raw material particle residence time, and kiln tail flue gas temperature were optimized using response surface analysis. The best combination of process parameters was obtained as $n(\text{CaSO}_4)/n(\text{S}_2) = 3.04$. The raw material particle residence time and kiln tail flue gas temperature were 8.90 s and 1265.39 K, respectively. The simulation experiment verified that the CaSO_4 decomposition rate reached 23.24%, with a relative error of 1.69%. This was 9.64% higher than that before optimization, thereby proving the validity of the established model.

Author Contributions: Conceptualization, Y.C. and X.F.; methodology, X.F.; software, L.Z.; validation, B.Z., X.F. and L.Z.; formal analysis, Y.C.; investigation, X.F.; data curation, Y.C.; writing—original draft preparation, X.F.; writing—review and editing, Y.C.; visualization, B.Z.; supervision, Y.C.; project administration, Y.C.; funding acquisition, Y.C. All authors have read and agreed to the published version of the manuscript.

Funding: This work was funded by the National Key R&D Program of China (No. 2016YFB0303400), grant number 2016YFB0303400.

Data Availability Statement: Not applicable.

Acknowledgments: The authors are grateful to the National Key R&D Program of China (2016YFB0303400). All individuals included in this section have consented to the acknowledgement.

Conflicts of Interest: The authors declare no conflict of interest.

References

1. Wei, Z.; Deng, Z. Research hotspots and trends of comprehensive utilization of phosphogypsum: Bibliometric analysis. *J. Environ. Radioactiv.* **2022**, *242*, 106778. [[CrossRef](#)]
2. Gao, J.; Li, Q.; Liu, F. Calcium sulfate whisker prepared by flue gas desulfurization gypsum: A physical–chemical coupling production process. *Chin. J. Chem. Eng.* **2020**, *28*, 2221–2226. [[CrossRef](#)]
3. Zhang, J.; Wei, C.; Ran, J.; Li, Y.; Chen, J. Properties of polymer composite with large dosage of phosphogypsum and its application in pipeline. *Polym. Test.* **2022**, *116*, 107742. [[CrossRef](#)]
4. Xiao, J.; Lu, T.; Zhuang, Y.; Jin, H. A Novel Process to Recover Gypsum from Phosphogypsum. *Materials* **2022**, *15*, 1944. [[CrossRef](#)]
5. Isteri, V.; Ohenoha, K.; Hanein, T.; Kinoshita, H.; Kletti, H.; Rößler, C.; Tanskanen, P.; Illikainen, M.; Fabritius, T. Ferritic calcium sulfoaluminate belite cement from metallurgical industry residues and phosphogypsum: Clinker production, scale-up, and microstructural characterization. *Cem. Concr. Res.* **2022**, *154*, 106715. [[CrossRef](#)]
6. He, W.; Hao, L.; Fan, C.; Li, S.; Lin, W. A two-step approach to phosphogypsum decomposition: Oxidation of CaS with CO_2 . *Thermochim. Acta.* **2022**, *708*, 179122. [[CrossRef](#)]
7. Yang, J.; Zhu, B.; Ma, L.; Liu, H. Investigation of Al_2O_3 and Fe_2O_3 transmission and transformation during the decomposition of phosphogypsum. *Chin. J. Chem. Eng.* **2019**, *27*, 1125–1131. [[CrossRef](#)]
8. Sun, L.; Zhao, Z.; Yang, X.; Sun, Y.; Li, Q.; Luo, C.; Zhao, Q. Thermochemical decomposition of phosphogypsum with Fe-P slag via a solid-state reaction. *Chin. J. Chem. Eng.* **2022**, *47*, 113–119. [[CrossRef](#)]
9. Antar, K.; Jemal, M. A thermogravimetric study into the effects of additives and water vapor on the reduction of gypsum and Tunisian phosphogypsum with graphite or coke in a nitrogen atmosphere. *J. Therm. Anal. Calorim.* **2018**, *132*, 113–125. [[CrossRef](#)]
10. Zhong, B.; Wang, X.; Zhang, Z.; Yang, X. New energy-saving and emission reduction process for sulfuric acid production from sulfur reduction decomposition of phosphogypsum. *Fertil. Ind.* **2014**, *41*, 7–10.
11. Ma, J.; Xu, J.; Liu, C.; Yi, Q.; Zheng, M.; Cheng, L.; Song, T. Chemical looping combustion of sulfur paste to SO_2 by phosphogypsum oxygen carrier for sulfur acid production. *Fuel* **2022**, *323*, 124386. [[CrossRef](#)]
12. Yang, X.; Zhang, Z.; Wang, X.; Yang, L.; Zhong, B.; Liu, J. Thermodynamic study of phosphogypsum decomposition by sulfur. *J. Chem. Thermodyn.* **2013**, *57*, 39–45. [[CrossRef](#)]
13. Wang, X.; Zhang, Z.; Yang, S.; Yang, X.; Zhong, B.; Hu, W.; Zhong, X. Sulfur decomposition phosphogypsum to sulfuric acid technology progress and promotion application. *Sulfuric Acid Ind.* **2018**, *280*, 45–49.
14. Ryan, J.; Bussmann, M.; DeMartini, N. CFD Modelling of Calcination in a Rotary Lime Kiln. *Processes* **2022**, *10*, 1516. [[CrossRef](#)]
15. Duan, S.; Li, B.; Rong, W. Numerical Simulation Study of Gas-Solid Heat Transfer and Decomposition Processes of Limestone Calcined with Blast Furnace Gas in a Parallel Flow Regenerative Lime Kiln. *Materials* **2022**, *15*, 4024. [[CrossRef](#)]
16. Lyu, H.; Lucas, D.; Rzehak, R.; Schlegel, F. A particle-center-averaged Euler-Euler model for monodisperse bubbly flows. *Chem. Eng. Sci.* **2022**, *260*, 117943. [[CrossRef](#)]
17. Mao, Y.; Zhang, D.; Chen, Z.; Jiang, Z.; Chen, X.; Deng, Y. Numerical modelling of multiphase FLOW and calcination process in an industrial calciner with fuel of heavy oil. *Powder Technol.* **2020**, *363*, 387–397. [[CrossRef](#)]
18. Yang, Y.; Zhang, Y.; Li, S.; Liu, R.; Duan, E. Numerical simulation of low nitrogen oxides emissions through cement precalciner structure and parameter optimization. *Chemosphere* **2020**, *258*, 127420. [[CrossRef](#)]

19. Nakhaei, M.; Grévain, D.; Jensen, L.S.; Glarborg, P.; Wu, H. NO emission from cement calciners firing coal and petcoke: A CPFD study. *Appl. Energy Combust. Sci.* **2021**, *5*, 100023. [[CrossRef](#)]
20. Gao, R.; Yin, S.; Song, T.; Lu, P. Numerical simulation of co-combustion of pulverized coal and biomass in TTF precalciner. *Fuel* **2023**, *334*, 126515. [[CrossRef](#)]
21. Ngamsidhipongsas, N.; Ponpesh, P.; Shotipruk, A.; Arpornwichanop, A. Analysis of the Imbert downdraft gasifier using a species-transport CFD model including tar-cracking reactions. *Energ. Convers. Manage.* **2020**, *213*, 112808. [[CrossRef](#)]
22. Zhang, W.; Xie, X.; Zhu, B.; Ma, Z. Analysis of phase interaction and gas holdup in a multistage multiphase rotodynamic pump based on a modified Euler two-fluid model. *Renew. Energ.* **2020**, *164*, 1496–1507. [[CrossRef](#)]
23. Carolin, K.; Roland, R. Investigation of Fluid-dynamics and Mass-transfer in a bubbly mixing layer by Euler-Euler simulation. *Chem. Eng. Sci.* **2022**, *264*, 118147.
24. Bhoopendra, P.; Yogesh, K.P.; Pratik, N.S. CFD analysis of the downdraft gasifier using species-transport and discrete phase model. *Fuel* **2022**, *328*, 125302.
25. Mei, S.; Xie, J.; Chen, X.; Feng, H.; Jin, M. Numerical simulation of the complex thermal processes in a vortexing precalciner. *Appl. Therm. Eng.* **2017**, *125*, 652–661. [[CrossRef](#)]
26. Qiu, M.; Chen, Z.; Jiang, L.; Liu, R.; Tang, Y.; Liu, M. Numerical simulation of uranium tetrafluoride fluorination in a multistage spouted bed using the improved CFD-DEM chemical reaction model. *Particuology* **2023**, *75*, 119–136. [[CrossRef](#)]
27. Menter, F.R. Higher, Order Turbulence Model Predictions for Complex 2D and 3D Flowfields. In *Engineering Turbulence Modelling and Experiments*; Elsevier: Amsterdam, The Netherlands, 1993; pp. 229–238.
28. Jin, W.; Xiao, J.; Ren, H.; Li, C.; Zheng, Q.; Tong, Z. Three-dimensional simulation of impinging jet atomization of soft mist inhalers using the hybrid VOF-DPM model. *Powder Technol.* **2022**, *407*, 117622. [[CrossRef](#)]
29. Fooladgar, E.; Brackmann, C.; Mannazhi, M.; Ögren, Y.; Bengtsson, P.; Wiinikka, H.; Tóth, P. CFD modeling of pyrolysis oil combustion using finite rate chemistry. *Fuel* **2021**, *299*, 120856. [[CrossRef](#)]
30. Talice, M.; Juretić, F.; Lahaye, D. Turbulent Non-Stationary Reactive Flow in a Cement Kiln. *Fluids* **2022**, *7*, 205. [[CrossRef](#)]
31. Sohn, H.Y.; Szekely, J. The effect of intragrain diffusion on the reaction between a porous solid and a gas. *Chem. Eng. Sci.* **2015**, *29*, 630–634. [[CrossRef](#)]
32. Szekely, J.; Evans, J.W.; Sohn, H.Y. *Gas-Solid Reactions*, 1st ed.; Academic Press: New York, NY, USA, 1976; pp. 101–105.
33. Borgwardt, R.H. Calcination kinetics and surface area of dispersed limestone particles. *Aiche. J.* **1985**, *31*, 103–111. [[CrossRef](#)]
34. Keener, S.; Khang, S.J. A Structural Pore Development Model for Calcination. *Chem. Eng. Commun.* **1992**, *117*, 279–291. [[CrossRef](#)]
35. Li, Z.; Cai, N. *Principle of Gas-Solid Reaction*, 1st ed.; Science Press: Beijing, China, 2020.
36. Mo, D. *Metallurgical Kinetics*, 1st ed.; Central South University of Technology Press: Beijing, China, 1987; pp. 193–208.
37. Yan, Z.; Wang, Z.; Wang, X.; Liu, H.; Qiu, J. Kinetic model for calcium sulfate decomposition at high temperature. *T. Nonferr. Metal. Soc.* **2015**, *25*, 3490–3497. [[CrossRef](#)]
38. Khinast, J.; Brunner, C.; Staudinger, G.; GF, K. Decomposition of limestone-The influence of CO₂ and particle size on the reaction rate. *Chem. Eng. Sci.* **1996**, *4*, 51. [[CrossRef](#)]
39. Satterfield, C.N.; Feakes, F. Kinetics of the thermal decomposition of calcium carbonate. *Aiche J.* **2010**, *5*, 115–122. [[CrossRef](#)]
40. Bohnstein, M.V.; Langen, J.; Frigge, L.; Stroh, A.; Jochen, S.; Epple, B. Comparison of CFD Simulations with Measurements of Gaseous Sulfur Species Concentrations in a Pulverized Coal Fired 1 MWth Furnace. *Energy Fuels* **2016**, *30*, 9836–9849. [[CrossRef](#)]
41. Ye, D.; Hu, J. *Handbook of Applied Inorganic Thermodynamics Data*, 2nd ed.; Metallurgical Industry Press: Beijing, China, 2002.

Disclaimer/Publisher’s Note: The statements, opinions and data contained in all publications are solely those of the individual author(s) and contributor(s) and not of MDPI and/or the editor(s). MDPI and/or the editor(s) disclaim responsibility for any injury to people or property resulting from any ideas, methods, instructions or products referred to in the content.